Cell Reports

Article

Nucleoporin-93 reveals a common feature of aggressive breast cancers: robust nucleocytoplasmic transport of transcription factors

Graphical abstract

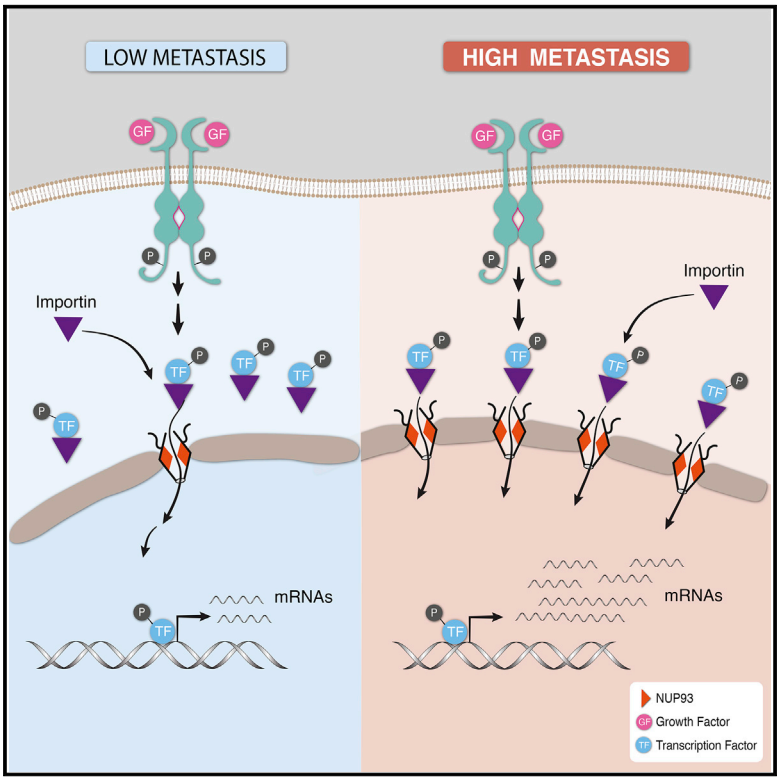

Highlights

- Multi-omics pipelines associate NUP93 overexpression with aggressive breast cancers
- NUP93 enhances nuclear transport of specific metastasis mediators (e.g., β-catenin)
- Peptides inhibiting translocation of these mediators inhibit metastasis in animals
- Unblocked nucleocytoplasmic transport emerges as a hallmark of advanced cancers

Authors

Nishanth Belugali Nataraj, Ashish Noronha, Joo Sang Lee, ..., Rony Seger, Eytan Ruppin, Yosef Yarden

Correspondence

yosef.yarden@weizmann.ac.il

In brief

Nataraj et al. develop multi-omics pipelines, which uncover critical roles of nucleoporin-93 (NUP93), a component of the nuclear pore complex, in metastasis of breast cancer. NUP93 overexpression in aggressive tumors unblocks nucleocytoplasmic transport of several transcription mediators, including β-catenin. Accordingly, specific inhibitors of NUP93-assisted transport can reduce metastasis.

Nataraj et al., 2022, Cell Reports *38*, 110418
February 22, 2022 © 2022
https://doi.org/10.1016/j.celrep.2022.110418

CellPress

Cell Reports

CellPress
OPEN ACCESS

Article

Nucleoporin-93 reveals a common feature of aggressive breast cancers: robust nucleocytoplasmic transport of transcription factors

Nishanth Belugali Nataraj,[1] Ashish Noronha,[1] Joo Sang Lee,[2] Soma Ghosh,[1] Harsha Raj Mohan Raju,[3] Arunachalam Sekar,[1] Binyamin Zuckerman,[1] Moshit Lindzen,[1] Emilio Tarcitano,[1] Swati Srivastava,[1] Michael Selitrennik,[4] Ido Livneh,[5] Diana Drago-Garcia,[1] Oscar Rueda,[6] Carlos Caldas,[6] Sima Lev,[3] Tamar Geiger,[3,4] Aaron Ciechanover,[5] Igor Ulitsky,[1] Rony Seger,[1] Eytan Ruppin,[2] and Yosef Yarden[1,7,*]

[1]Department of Biological Regulation, Weizmann Institute of Science, Rehovot, Israel
[2]Cancer Data Science Lab, National Cancer Institute, NIH, Rockville, MD, USA
[3]Department of Molecular Cell Biology, Weizmann Institute of Science, Rehovot, Israel
[4]Department of Human Molecular Genetics and Biochemistry, Sackler Faculty of Medicine, Tel Aviv University, Tel Aviv, Israel
[5]Technion Integrated Cancer Center (TICC) and the Rappaport Faculty of Medicine and Research Institute, Technion-Israel Institute of Technology, Haifa, Israel
[6]Cancer Research UK Cambridge Institute, University of Cambridge and the Cambridge Cancer Centre, Department of Oncology, Cambridge, UK
[7]Lead contact
*Correspondence: yosef.yarden@weizmann.ac.il
https://doi.org/10.1016/j.celrep.2022.110418

SUMMARY

By establishing multi-omics pipelines, we uncover overexpression and gene copy-number alterations of nucleoporin-93 (NUP93), a nuclear pore component, in aggressive human mammary tumors. NUP93 overexpression enhances transendothelial migration and matrix invasion *in vitro*, along with tumor growth and metastasis in animal models. These findings are supported by analyses of two sets of naturally occurring mutations: rare oncogenic mutations and inactivating familial nephrotic syndrome mutations. Mechanistically, NUP93 binds with importins, boosts nuclear transport of importins' cargoes, such as β-catenin, and activates MYC. Likewise, NUP93 overexpression enhances the ultimate nuclear transport step shared by additional signaling pathways, including TGF-β/SMAD and EGF/ERK. The emerging addiction to nuclear transport exposes vulnerabilities of NUP93-overexpressing tumors. Congruently, myristoylated peptides corresponding to the nuclear translocation signals of SMAD and ERK can inhibit tumor growth and metastasis. Our study sheds light on an emerging hallmark of advanced tumors, which derive benefit from robust nucleocytoplasmic transport.

INTRODUCTION

Breast carcinoma is the leading cause of cancer-related mortality in women. Owing to genomic instability, breast cancers often exhibit somatic copy number aberrations (CNAs) (Dawson et al., 2013), such as amplification of *RBB2*/*HER2* (Slamon et al., 1989). By means of heterodimer formation with the epidermal growth factor receptor (EGFR), ERBB2/HER2 acts as an amplifier of growth factor signals (Yarden and Pines, 2012). Importantly, kinase inhibitors and combinations of antibodies that inhibit human EGFR 2 (HER2) are widely used to treat HER2-overexpressing breast cancers (Baselga and Swain, 2010), which exemplifies the therapeutic potential offered by the identification of overexpressed proteins. Because many other cellular functions rely on multi-protein complexes, precise and timely dosage of the individual elements, especially protein stoichiometry, might be critical and define true driver genes (Lalanne et al., 2018). For example, gene dosage imbalance and limited CNAs affecting diverse breast cancer genes, all regulating receptor endocytosis, confer poor prognosis (Mueller et al., 2018).

Here, we demonstrate that breast cancers acquire aggressive phenotypes when another trafficking pathway, which regulates cytoplasm-to-nucleus transport of active transcription factors, undergoes aberrant activation. In general, small molecules passively diffuse into the nucleus, whereas passage of large molecules is facilitated by binding with transport proteins (importins). Usually, cargo proteins shuttle to the nucleus when an intrinsic nuclear localization signal interacts with an importin, which escorts cargo to the nucleus via the large nuclear pore complex (NPC; ~110 MDa) (Knockenhauer and Schwartz, 2016). Alternatively, activated signaling proteins such as ERK translocate across the NPC by means of specific nuclear translocation signals (NTS) (Maik-Rachline et al., 2019). The NPC structure, which consists of ~1,000 protein subunits

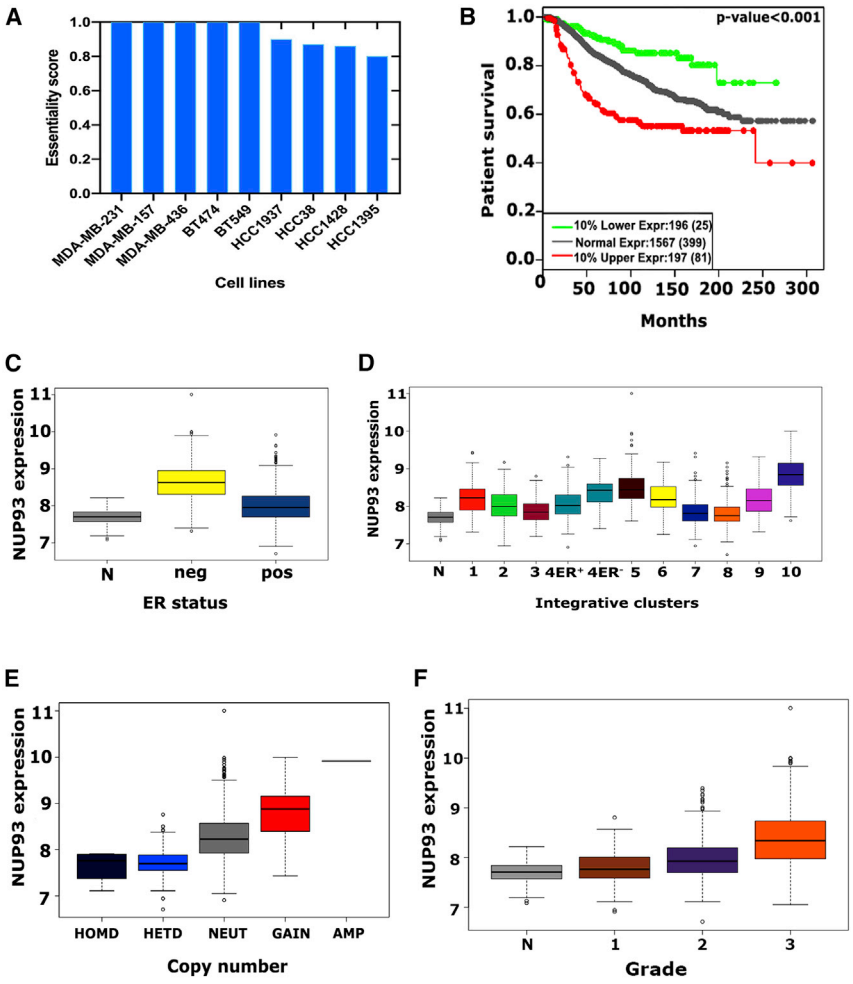

Figure 1. NUP93 is essential for survival of breast cancer and its abundance associates with shorter patient survival

(A) Four cell lines for which NUP93 is least essential, along with 5 of the 24 cell lines for which the predicted essentiality is maximal.

(B) Kaplan-Meier survival curves based on the METABRIC dataset and *NUP93* expression levels.

(C) Analysis of NUP93 expression according to ER status: positive, negative, and neutral (N).

(D) Analysis of *NUP93* expression in the ten integrative clusters of breast cancer.

(E) Correlation between NUP93 gene copy number and mRNA expression based on array comparative genome hybridization. AMP, amplification; NEUT, neutral; HETD, heterozygous deletion; HOMD, homozygous deletion.

(F) Distribution of NUP93 gene expression and grade of breast cancers.

(nucleoporins), is stabilized by protein complexes arranged in concentric rings.

Using a multi-omics pipeline, we identified a specific component of the inner NPC's ring, nucleoporin-93 (NUP93), as highly essential for breast cancer. Loss-of-function (LOF) mutations affecting NUP93 are recognized as monogenic causes of steroid-resistant nephrotic syndromes (SRNS) (Braun et al., 2016), whereas rare gain-of-function (GOF) mutations identify relatively aggressive mammary tumors (Lee et al., 2016). In line with these observations, we report that elevated abundance of NUP93, in similarity to rare GOF mutations, promotes growth and metastasis of mammary tumors, whereas LOF mutations, similar to *NUP93* knockdown, can markedly retard cancer progression in animal models. Subcellular fractionation and heterokaryon analyses revealed that NUP93 overexpression enhances the concluding step of transcription factor translocation to the nucleus, an event shared by several oncogenic signaling pathways, including those stimulated by WNT and EGF. Focusing on WNT, we report that NUP93 binds with importins, accelerates nuclear transport of β-catenin, and activates MYC. Accordingly, NTS-mimetic decoy peptides inhibited tumor progression in animal models. These results identify a robust, yet targetable, mechanism shared by aggressive tumors that depend on persistent signaling from the tumor microenvironment to the nucleus.

RESULTS

NUP93 is essential for survival of mammary tumor cells, and its abundance associates with poor prognosis of patients with aggressive subtypes of breast cancer

To identify genes relevant to breast cancer progression, we integrated four types of computational data: RNA sequencing (RNA-seq) data from patient datasets, recurrent somatic CNAs, patient survival data, and gene essentiality scores derived from whole-genome short hairpin RNA (shRNA) screens (Cheung et al., 2011). Combining the top 500 clinically relevant genes and the 500 most essential genes yielded a ranked list of 20 genes (Table S1). Interestingly, two tubulin genes topped the list, in line with reports linking tubulins to poor patient survival (Kanojia et al., 2015). The scores received by NUP93 were close to those received by the tubulins. Figure 1A presents the scores received by NUP93 in a series of breast cancer cell lines. Because anti-tubulin drugs are widely used but no anti-cancer drugs target NUP93, we focused on the nucleoporin. Additional analyses validated that overexpression of NUP93 associates with poor patient prognosis (log-rank $p < 3.61e{-}12$), especially prognosis of patients with triple-negative and HER2-positive tumors. As examples, we divided these groups in the METABRIC dataset (Curtis et al., 2012) into three categories according to *NUP93* expression levels. The survival analyses separately performed for each group verified that *NUP93* overexpression is independently and significantly associated with shorter disease-free survival in both subtypes (Figures 1B and S1A). The same dataset was also stratified according to the status of estrogen receptor (ER) (Figure 1C), which revealed that the

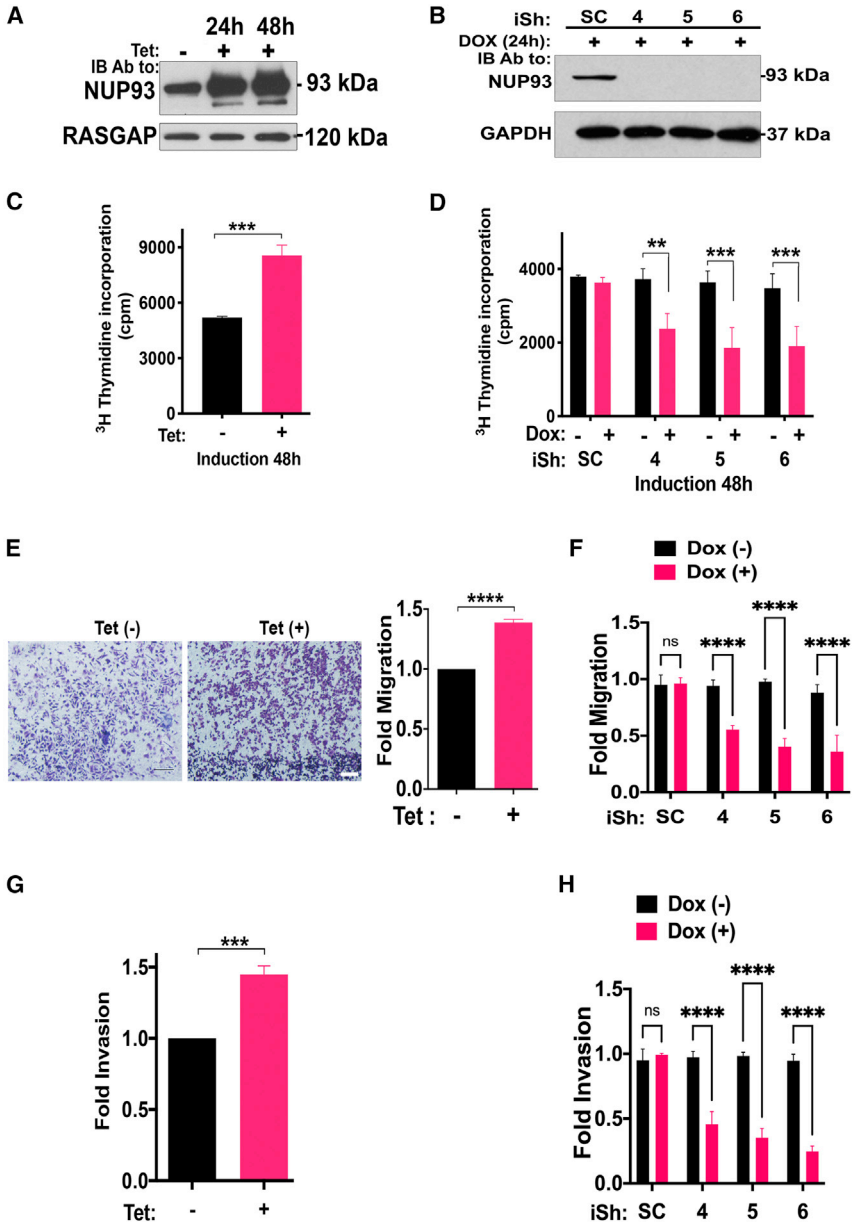

Figure 2. NUP93 overexpression (or knockdown) promotes (or inhibits) DNA synthesis, migration, and matrix invasion

(A and B) MDA-MB-231 cells overexpressing a Tet-inducible NUP93 (A) or DOX-inducible shRNAs specific to NUP93 (B) were exposed to the inducer prior to immunoblotting. SC, scrambled shRNA.

(C and D) Rates of DNA synthesis were determined using the [^{3}H]thymidine incorporation assay following induction for 48 h. Shown are means ± SEM.

(E–H) Cells expressing a Tet-inducible NUP93 (E and G) or DOX-inducible shNUP93 (F and H) were treated with the inducer for 48 h and later subjected to migration (E and F) or invasion (G and H) assays. Migrated or invaded cells were photographed and quantified. Scale bar, 100 μm.

All experiments used triplicates and are representative of at least three independent experiments. ***$p \leq 0.001$, ****$p \leq 0.0001$.

more aggressive group of tumors, which lacks ER expression, displayed relatively high NUP93.

An association between NUP93 and more virulent mammary tumors similarly emerged from analysis of the ten integrative clusters (ICs) of breast cancer (Dawson et al., 2013). IC10, which incorporates mostly triple-negative tumors, showed highest expression (Figure 1D). Likewise, *NUP93*'s transcripts were relatively high in IC5, which identifies almost all cases with *HER2* amplification. In addition, we found that high NUP93 was significantly associated with CNA (Figure 1E). As expected, the highest gains of this gene were found in the basal subtype. Furthermore, high NUP93 expression was typical to high-grade tumors (Figure 1F). In conclusion, by developing a multi-omics pipeline, we learned that a component of the NPC is essential for survival of breast cancer cells, and its abundance predicts poor prognosis of the relatively aggressive disease subtypes.

Inducible overexpression and downregulation reveal involvement of NUP93 in mammary cell proliferation and invasion

Because NUP93 is overexpressed in the basal subtype, we selected two basal models: MDA-MB-231 cancer cells and MCF10A, a non-tumorigenic immortalized line. First, we expressed an inducible allele of NUP93 in MDA-MB-231 cells and verified overexpression (ox) post induction with tetracycline (Tet) (Figure 2A). Reciprocally, we established sublines expressing different doxycycline (DOX)-inducible shRNAs (iSh) (Figure 2B). As predicted, exposing cells to Tet enhanced their ability to incorporate a radioactive nucleoside into DNA (Figure 2C), whereas DOX-induced downregulation reduced DNA synthesis (Figure 2D). Next, we applied a cell viability assay, which supported the ability of NUP93 to enhance viability (Figures S1B and S1F). Similar conclusions were derived from experiments that used subclones constitutively expressing shNUP93, and cells expressing small interfering RNAs (siRNAs) specific to NUP93 (Figures S1C and S1G, right). In parallel we similarly established derivatives of MCF10A cells (Figures S1D and S1E), which confirmed the association between viability and NUP93 levels and were later used for additional assays (see below).

According to a recent breast cancer study, predictors of migration, rather than proliferation, are more strongly associated with patient survival (Nair et al., 2019). When we placed inducible MDA-MB-231 cells on the upper compartment of cell-culture

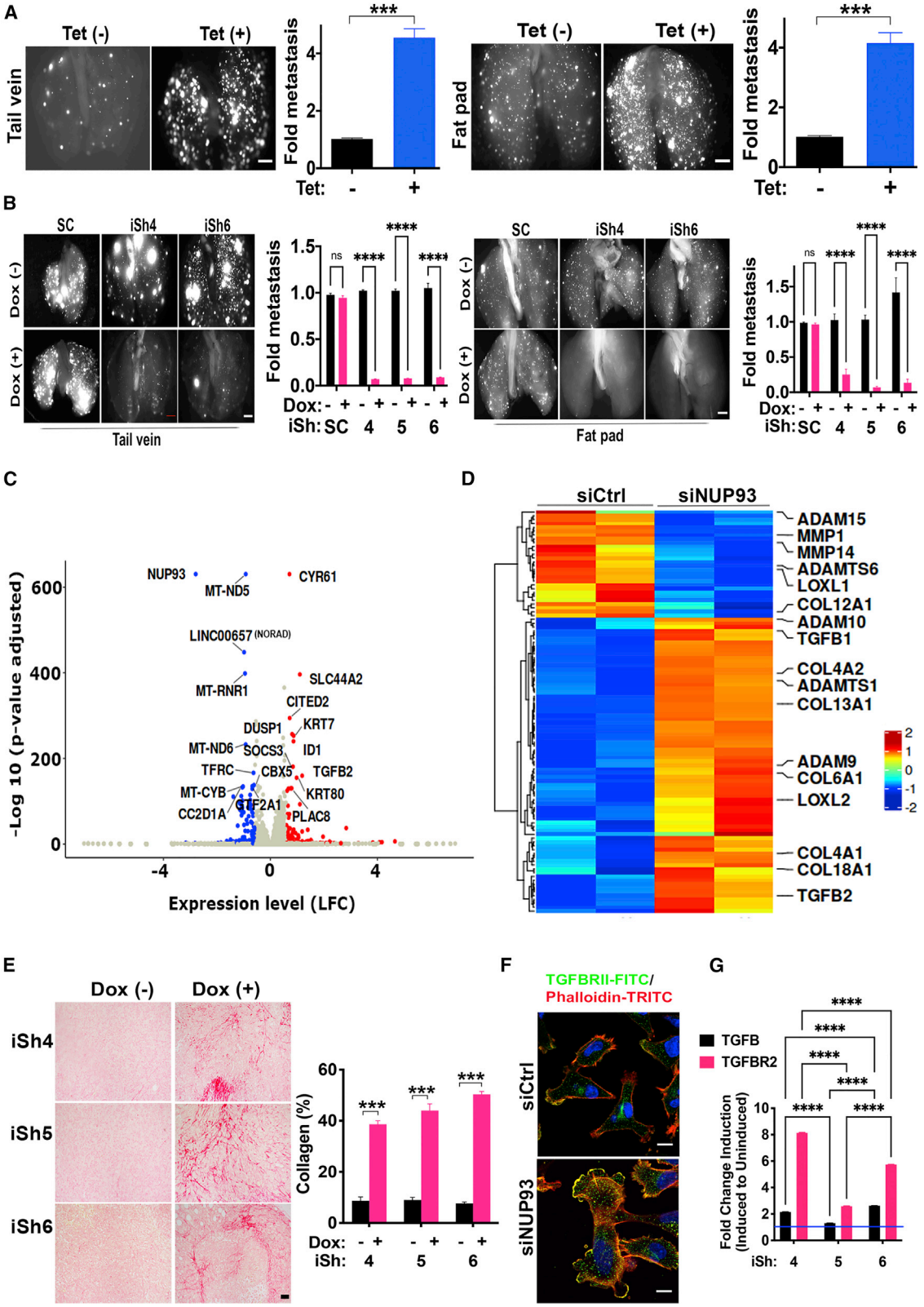

(legend on next page)

inserts and treated them with the inducer, they migrated significantly faster than untreated cells (Figure 2E). The reciprocal approach, which used DOX-inducible shRNAs, confirmed relatively low migration rates (Figure 2F). Moreover, when the intervening membrane was coated with an extracellular matrix, we similarly observed increased and decreased invasion rates when cells were exposed to Tet or DOX, respectively (Figures 2G and 2H). Additional migration and invasion assays (Figures S1H and S1I) further supported the ability NUP93 to increase motility. As expected, immunofluorescence (Figure S1J) and electron microscopy (Figure S1K) indicated that the density of nuclear pores was reduced or increased in NUP93-depleted or NUP93-overexpressing cells, respectively. In conclusion, in line with essentiality and clinical significance, high abundance of NUP93 can enhance *in vitro* several attributes of the transformed phenotype. This feature is specific to NUP93, since siRNAs specific to other components of the NPC (i.e., NUP62, NUP98, and NUP107) could not regulate DNA synthesis (Figure S2A).

NUP93 overexpression augments transendothelial migration and remodels focal adhesion sites

A recent report implicated *NUP93* in actin cytoskeleton reorganization and stress fiber formation (Bersini et al., 2020). Indeed, when pre-formed mammary spheroids were induced with tetracycline (to elevate NUP93), many cells migrated outward and formed invasion zones (Figure S2B). Reciprocally, NUP93 silencing reduced zone area (Figure S2C). Altered invasiveness emerged also from transendothelial migration assays that overlaid endothelial monolayers with cells expressing an inducible shNUP93 (Figure S2D). Interestingly, depletion of NUP93 increased cell area (Figure S2E) and reduced by 4-fold the ability of cells to form invasive actin-filled protrusions, called invadopodia (Figure S2F). Notably, invadopodia contain dynamic microdomains of actin-rich adhesion sites (Paterson and Courtneidge, 2018). Accordingly, depletion of NUP93 was associated with remodeling of actin cables (Figure S2G). In addition, in line with the report by Bersini et al. (2020), we observed increased expression of endothelin (EDN1), which is involved in cytoskeleton and extracellular matrix (ECM) remodeling, but another gene they reported, LIMCH1, was unaffected (Figure S2H). Likewise, we observed upregulation of specific integrins in shNUP93-treated cells (Figure S2I). Hence, we extended the analysis to two paxillin family members, paxillin and Hic-5, which are involved in turnover of adhesion sites (Petropoulos et al., 2016). Imaging unveiled redistribution, along with upregulation of the respective areas in siNUP93-treated cells (Figure S2J). In summary, following overexpression NUP93 increases three-dimensional invasion, enhances transendothelial migration and invadopodium assembly, and remodels adhesion sites.

In animal tumor models, high NUP93 associates with accelerated growth and metastasis

Next, we implanted MDA-MB-231 cells expressing a Tet-inducible NUP93 allele in the fat pad of female mice, and added the inducer to the drinking water of one of two groups of mice. Both the volumes and weights of tumors we harvested 3 weeks later were significantly larger in the treated group (Figure S3A). A reciprocal experiment, which made use of cells expressing a DOX-inducible shNUP93, reinforced the ability of NUP93 to accelerate tumor growth (Figure S3B). This conclusion was independently supported by using cells stably expressing shNUP93s (Figure S3C). As an initial test of metastasis, lungs were excised and metastases were quantified (Figure S3D). The results reflected strong inhibitory effects, which prompted assays employing inducible overexpression. The corresponding cells were injected either into the tail vein (Figure 3A, left) or into the subaxillary mammary fat pad (Figure 3A, right). Seven days later, we added tetracycline to the drinking water of some mice and sacrificed all animals 3 weeks later. The results indicated that NUP93 overexpressers are endowed with >3-fold stronger capacity to colonize lungs. Furthermore, when using tumors expressing shNUP93, we observed remarkably fewer lung metastases (Figure 3B). Together, these observations assigned to NUP93 an important role in metastasis.

To uncover the identity of protein mediators, we sequenced RNA from MDA-MB-231 cells that were pre-treated with siNUP93. The major differentially expressed (DE) genes are shown in Figure 3C and Data S1. Along with upregulation of CYR61, a target of transforming growth factor β (TGF-β) (Bartholin et al., 2007), we observed downregulation of several mitochondrial genes, such as two subunits of the respiratory chain I, and RNR1, a subunit of ribonucleotide reductase, which catalyzes deoxynucleotide triphosphate (dNTP) synthesis. We also noted changes in TGF-β and ECM components (Hynes and Naba, 2012). Interestingly, while some of the DE genes we identified overlapped a previously reported set (Bersini et al., 2020), other genes differed, probably due to technical reasons. The heatmap shown in Figure 3D lists the major altered matrisome

Figure 3. NUP93 abundance associates with increased metastasis and low expression of matrisome components

(A) MDA-MB-231-RFP cells inducibly overexpressing NUP93 were injected into either the tail vein (2×10^4 cells, left) or the subaxillary mammary fat pad (2×10^6 cells; right) of mice. One week later, tetracycline (3 mg/mL) was added to the drinking water and mice were sacrificed 3 weeks later. Shown are fluorescence images of lungs and quantification of metastases. Data are representative of at least two experiments, which used six mice per experimental arm. Scale bar, 0.5 cm.

(B) Cells inducibly expressing shNUP93 were injected into the tail vein or the subaxillary mammary fat pad as in (A). Data are representative of 2–3 experiments. Each experimental arm included six mice.

(C and D) RNA from siCtrl- and siNUP93-treated MDA-MB-231 cells was sequenced. Differentially expressed genes are presented in a scatterplot (C) and a heatmap (D; matrisome genes). Data were derived from one experiment that used two technical repeats.

(E) Tumors from (B) were stained with picrosirius red, and images were captured and quantified (averages ± SEM).

(F) Cells pre-treated with control or siNUP93 were stained for TGFBRII (green) and F-actin (red). Scale bar, 10 μm.

(G) Cells expressing different inducible shNUP93 (iSh) were incubated for 48 h in the absence or presence of the inducer (DOX). Media were assayed for TGF-β and extracts were tested for TGFBRII using ELISA. Data are representative of three independent experiments that were performed in triplicates.

***$p \leq 0.001$, ****$p \leq 0.0001$ in (A), (B), (E), and (G).

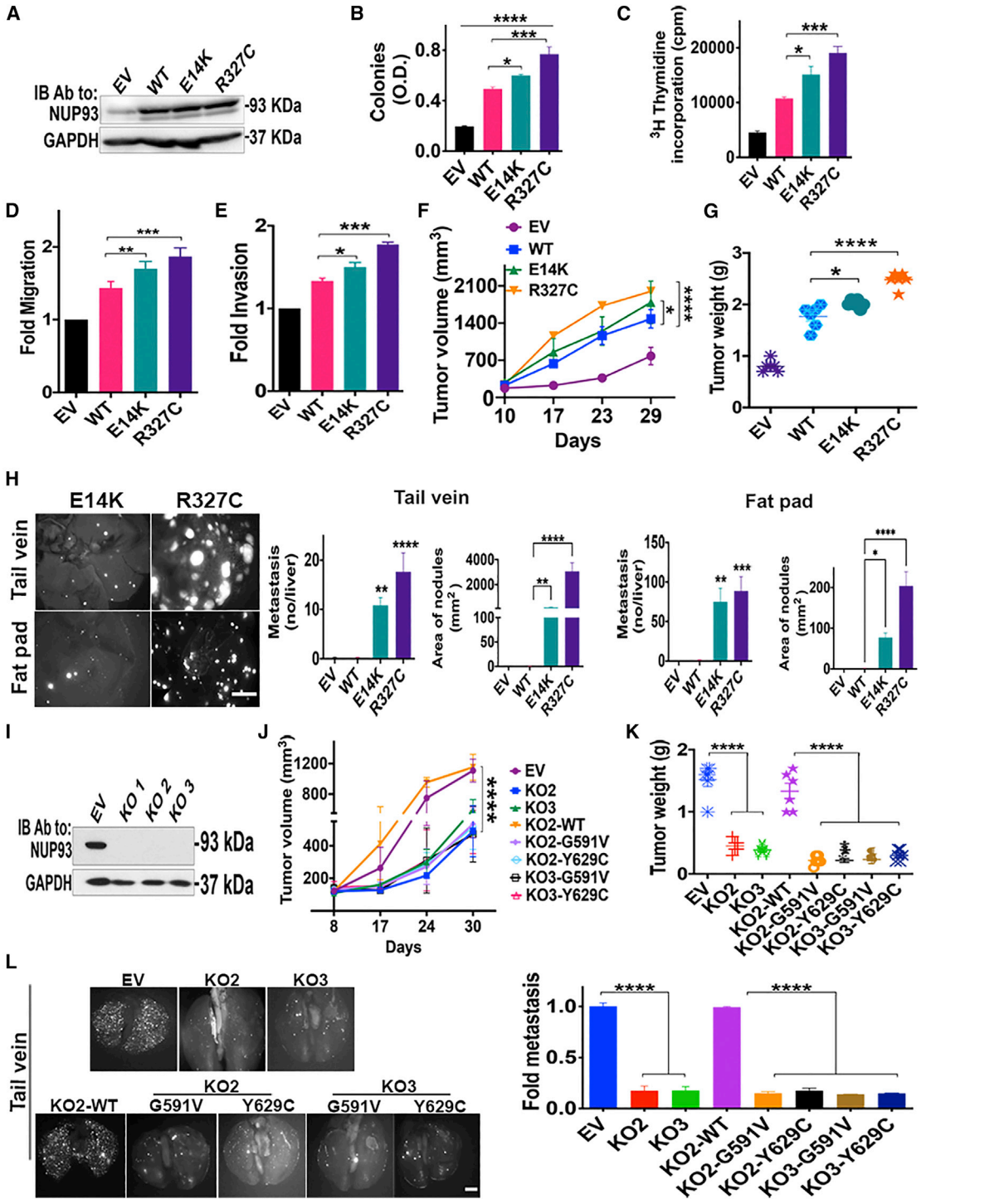

Figure 4. Naturally occurring gain- and loss-of function mutants of NUP93 respectively enhance or inhibit oncogenesis

(A) MDA-MB-231 cells pre-transfected with the indicated NUP93-encoding vectors (EV, empty vector) were selected and extracts immunoblotted (IB) using specific antibodies.

(B) The sublines from (A) were sparsely seeded in triplicates, fixed, and colonies stained 10 days later. The experiment was repeated twice.

(C–E) The four sublines were subjected to a DNA synthesis assay (C), cell migration assay (D), or invasion assay (E), and averages of triplicates are shown. All experiments were repeated at least twice.

(F and G) Cells from A (2 × 10^6) were implanted in the fat pad of female mice. Tumor volumes are presented in (F). Tumors were excised on day 30 and their weights were determined (G). The experiment was repeated twice, and each experimental arm included six animals.

(legend continued on next page)

genes. These observations were supported by means of PCR (Figure S3E) and immunoblotting for collagen IVa6 (Figure S3F). Because collagen enables cell-to-matrix adhesion through binding with integrins, we predicted changes in substrate adhesion. Experiments using DOX-inducible shNUP93 (Figure S3G) or a Tet-inducible NUP93 (Figure S3H) confirmed that NUP93 overexpression reduces substrate adhesion (note that the inducers were added 48 h before the actual adhesion assays). To examine collagens, we stained collagen IVa6 (Figure S3I) and detected collagen fibrils only in NUP93-depleted cells. Next, tumors excised from DOX-treated mice were stained with either a collagen dye, picrosirius red (Figure 3E), or an anti-collagen IVa6 antibody (Figure S3J). Evidently, shNUP93 tumors showed strong staining only if the animals were pre-treated with DOX. Since collagen is induced by TGF-β (Chen et al., 2006), we probed for the ligand and the receptor, TGFBRII. The results indicated co-induction, along with localization of TGFBRII to lamellipodia (Figures 3F, 3G, and S3K–S3M). Additional results, which are not presented, implicated the TGF-β target, CYR61, along with the YAP pathway, in the accelerated spreading displayed by NUP93-depleted cells. In conclusion, high NUP93 confers growth and metastasis through a mechanism involving increased nucleotide metabolism, weakening adhesion to ECM and reducing secretion of TGF-β.

Naturally occurring gain- and loss-of-function mutations confirm NUP93's roles in metastasis

Several NUP93 mutations were identified by a large-scale screen aimed at putative driver mutations of metastasis (Lee et al., 2016). Hence, we stably expressed two mutant alleles in MCF10A (Figure S4A) and MDA-MB-231 cells (Figure 4A). Both mutants, especially R327C, superseded the ability of wild-type (WT) NUP93 to seed colonies (Figures 4B and S4B). In addition, we performed DNA synthesis (Figures 4C and S4C) and migration and invasion assays (Figures 4D, 4E, S4D, and S4E), which indicated that the mutants were more active than the WT form. Next, we implanted the respective MDA-MB-231 cells in the fat pad of animals and followed tumor growth (Figures 4F and 4G). Both mutations enhanced tumor growth relative to WT and control (empty vector) cells. Similarly, quantification of metastatic lung nodules indicated that both mutants were more active than WT in two metastasis assay formats (Figure S4F). Notably, we occasionally observed metastases in other organs. Focusing on liver metastases, we observed interesting differences (Figure 4H): whereas cells overexpressing either mutant colonized livers, we were unable to detect hepatic lesions in mice injected with WT-NUP93-overexpressing cells. In conclusion, GOF NUP93 mutations enhance oncogenic attributes in animal models and confer organ-specific metastasis.

Analyses of patients with nephrotic syndromes detected homozygous missense NUP93 mutations (Braun et al., 2016). To study their impact on oncogenesis, we firstly disrupted the endogenous *NUP93* gene using CRISPR/Cas9. Several knockout (KO) clones were established (Figure 4I). Next, we generated a series of KO cells expressing WT or individual mutants (Figure S4G). As expected, all KO sublines exhibited reduced viability and DNA synthesis (Figures S4H and S4I), as well as relatively low motility and high adhesion (Figures S4J–S4L). Furthermore, unlike WT, neither mutant recovered normal migration/invasion rates in KO cells (Figures S4K and S4L). *In vivo* tests of tumor growth (Figures 4J and 4K) and metastasis (Figures 4L and S4M) supported the LOF phenotype: stable expression of neither mutant reconstituted the relatively high rates of tumor growth/metastasis displayed by KO cells re-expressing WT-NUP93. In summary, by studying naturally occurring GOF and LOF mutations, we obtained independent evidence supporting the critical roles played by NUP93 in breast cancer progression.

NUP93 overexpression activates RHO GTPases and enhances the WNT and other signaling pathways

RHO family guanosine triphosphatases (GTPases) serve as switches involved in mammary tumorigenesis (Zuo et al., 2016). Hence, we utilized the ability of effectors to bind with the corresponding GTP-bound forms. Overexpression of NUP93 increased CDC42-GTP and RAC1-GTP, but decreased RHOA-GTP (Figure S5A). Congruently, siNUP93 reduced active RAC1 and CDC42 but increased RHOA-GTP. Similarly, we observed significant downregulation of RAS-GTP in siNUP93-treated cells (Figure S5B). Because RAC1 and RAS integrate signals generated by multiple pathways, we undertook a promoter-reporter strategy. An NUP93 plasmid (Figure 5A) and siNUP93 (Figure S5C) were separately co-transfected into HEK293 cells with various luciferase reporters containing different DNA response elements (REs). siNUP93 decreased several signals and variably activated two collagen promoters, while NUP93 overexpression activated a surprisingly wide spectrum of promoters, including GRE (glucocorticoid RE), STAT, SMAD4, and FLI1. The strongest signal (>50-fold) was observed with a β-catenin reporter containing the binding site for the T cell factor (TCF/LEF). Nuclear accumulation of β-catenin is induced by WNT; once in the nucleus, β-catenin associates with TCF/LEF to activate target genes (Nusse and Clevers, 2017). In line with this, co-transfecting NUP93's oncogenic mutants increased reporter activity (Figure 5B) and β-catenin protein (Figure 5C), as well as increasing the expression of three β-catenin target genes (Figure S5D). Because EGF can transactivate the β-catenin pathway (Yang et al., 2011) and, similarly, SMAD3 can occupy WNT-responsive elements (Aloysius et al., 2018), we examined

(H) Cells from (A) were injected into either the tail vein (2×10^4 cells, upper images) or the fat pad (2×10^6 cells; lower images) of six mice. Metastatic liver nodules were quantified 4 weeks later. Shown are representative images of livers, along with image quantification. The experiments were repeated twice. Scale bar, 0.5 cm.

(I) CRISPR/Cas9 was used to ablate *NUP93* of MDA-MB-231 cells. Whole extracts were probed.

(J and K) Cells from (I) were injected into the fat pad of female mice. Likewise, individual KO clones stably re-expressing WT-NUP93, G591V-NUP93, or Y629C-NUP93 were implanted in mice. Mean tumor volumes (J) and weights (K) of the indicated groups (six mice per group) are presented. The experiment was repeated twice.

(L) Specific sublines were injected into the tail vein of female mice. Four weeks later, lungs were excised and metastatic nodules quantified. Shown are fluorescence images and quantification of lung metastases in all six mice of each group. The experiment was repeated twice. Scale bar, 0.5 cm. *, $p \leq 0.05$; **, $p \leq 0.01$; ***, $p \leq 0.001$; ****, $p \leq 0.0001$.

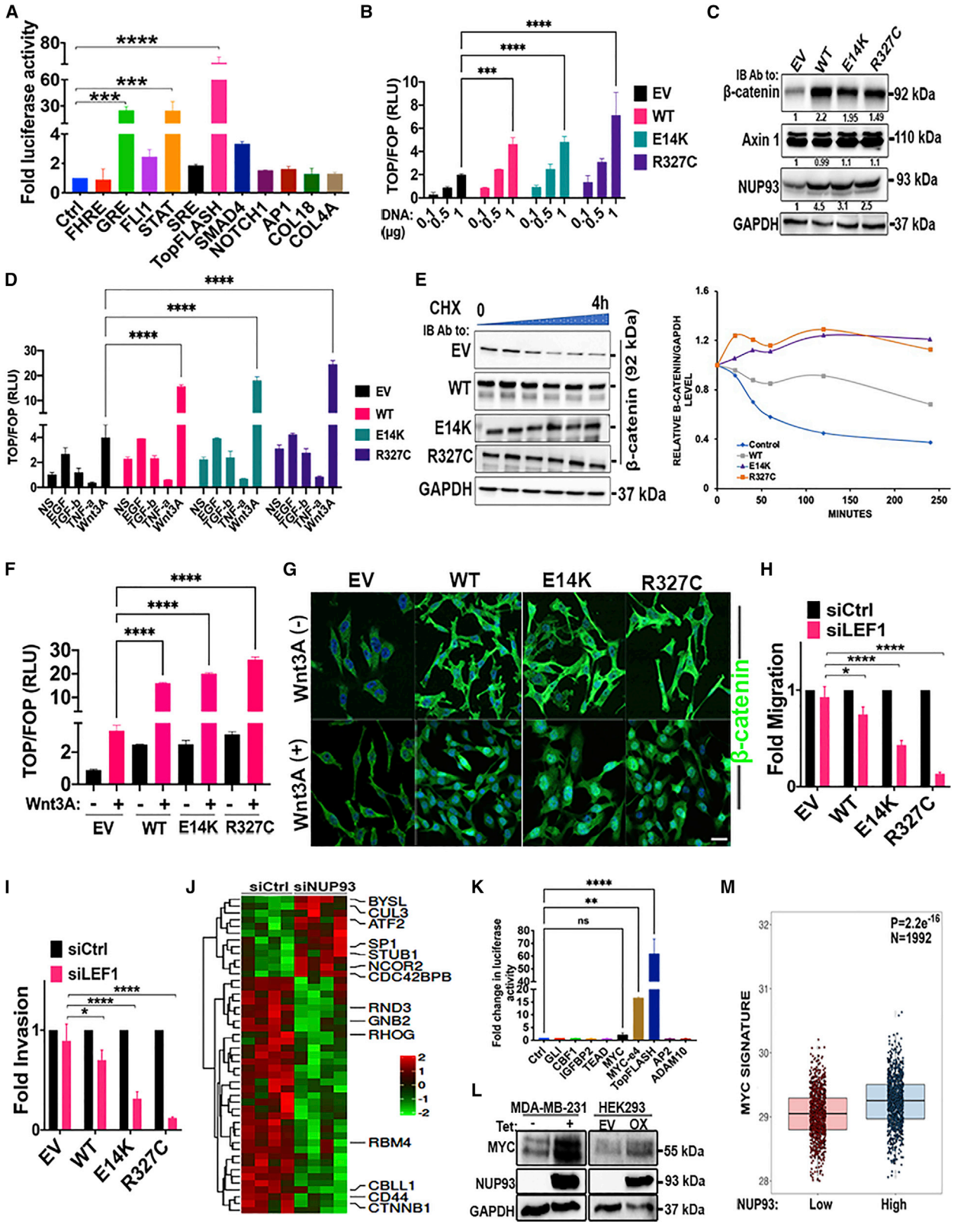

(legend on next page)

transactivation by EGF and TGF-β. The results confirmed transactivation and its enhancement by oncogenic NUP93s (Figure 5D). Next, we addressed effects on β-catenin stability. Treatment with cycloheximide confirmed the relatively short half-life of β-catenin (Figure 5E). In contrast, when overexpressed, both WT and oncogenic NUP93 mutants markedly prolonged β-catenin's stability, in line with complementary transcriptional and post-translational effects of NUP93 on β-catenin activation.

Using WNT3A, we found that R327C-NUP93, similar to WT, enhanced WNT3A-stimulated promoter activation (Figure 5F). To test whether this cooperative effect was due to increased nuclear transport of β-catenin, we firstly fractionated control cells and detected only a small fraction of β-catenin in the nucleus (Figure S5E). This fraction, however, was erased following NUP93 knockdown. Likewise, immunofluorescence indicated that treatment with WNT3A induced relatively weak nuclear translocation of β-catenin, which was enhanced following overexpression of WT and oncogenic NUP93 mutants (Figure 5G). The inferred pathway, WNT >> NUP93 >> β-catenin^{NUC} >> LEF1 >> target genes, was tested by depleting LEF1 (Figures 5H and 5I). While siLEF1 inhibited cell motility by approximately 30% in WT-NUP93 cells, this increased to 90% in R327C-NUP93 cells, in line with cooperativity and correctness of the inferred pathway. In conclusion, when overexpressed, NUP93 stabilizes β-catenin and enhances its nuclear transport, thereby augmenting the WNT pathway.

Proteome- and transcriptome-wide analyses identify β-catenin and MYC as targets of the overexpressed NUP93

To complement the analysis of promoters, we applied liquid chromatography-tandem mass spectrometry (LC-MS/MS) on subcellular fractions of siNUP93-treated cells (Figures 5J and S5F; Data S2), and confirmed that siNUP93 significantly reduced nuclear β-catenin. In addition, while the cytoplasmic fractions showed downregulation of MAPK pathways, the nuclear fractions supported the collagen effects described above. This was reflected by elevated levels of SP1, a collagen inducer (Li et al., 1995), cullin-3, which is essential for collagen export (Jin et al., 2012), and bystin, which regulates cell adhesion (Suzuki et al., 1998). Upregulation of all three proteins was confirmed, as well as their cytoplasm-to-nuclear translocations (Figures S5G and S5H).

While these observations revealed that NUP93 bottlenecks translocation of β-catenin to the nucleus, they left open the identity of the downstream targets. After forming a nuclear complex with TCF/LEF1, β-catenin activates transcription of several target genes, including the proto-oncogenes MYC and CCND1 (Herbst et al., 2014). Three lines of evidence indicated that NUP93 overexpression is coupled to strong activation of MYC.

(1) Reporter analyses that surveyed target genes of NOTCH (CBF1), Hedgehog (GLI1), and additional pathways indicated that activation of the MYC promoter was significantly higher in cells overexpressing NUP93 (Figure 5K). Notably, an MYC reporter also containing the corresponding enhancer displayed larger signals, indicating that the upstream enhancer might be more responsive to NUP93 than the respective promoter.
(2) Knocking down NUP93 inhibited transcription from both the β-catenin and MYC promoters (Figure S5I).
(3) In line with a previous report, which showed that tethering MYC alleles to the NPC by means of an oncogenic super-enhancer prolongs the half-life of MYC transcripts (Scholz et al., 2019), ectopic NUP93 strongly upregulated the 55 kDa MYC protein (Figure 5L).

To explore clinical relevance of the inferred NUP93-catenin-MYC axis, we divided the METABRIC dataset into two groups,

Figure 5. High expression of NUP93 stabilizes β-catenin, enhances its transcription and nuclear transport, and elevates MYC

(A) Cells were co-transfected with vectors encoding NUP93, pGL3 control plasmid, and the indicated luciferase reporters. Luminescence was quantified and normalized (means ± SEM; triplicates). The experiment was repeated thrice.

(B) Cells were transfected as in (A), except that FOPFlash and the indicated NUP93 plasmids were used. The experiment was repeated thrice.

(C) Immunoblotting and band quantification of extracts from cells overexpressing the indicated forms of NUP93.

(D) Cells were transfected as in (B), except that a 16 h incubation with the indicated ligands preceded luciferase assays. Shown are means (±SEM) of triplicates. The experiment was repeated thrice.

(E) The indicated NUP93 clones were pre-incubated with cycloheximide and lysates subjected to immunoblotting (left). β-Catenin bands were quantified and normalized (right). The experiment was repeated twice.

(F) HEK293 cells expressing specific NUP93 alleles, along with TOP/FOP and pGL3, were incubated for 16 h with medium from L cells expressing WNT3A or from control cells. Luminescence was quantified in triplicates and the experiment was repeated thrice.

(G) Cells stably expressing NUP93, the indicated mutants, or an empty vector (EV) were incubated with WNT3A medium as in (F) and probed for β-catenin 4 h later. The experiment was repeated thrice. Scale bar, 10 μm.

(H and I) Cells from (C) were pre-treated with siLEF1 and subjected 48 h later in triplicates to migration (H) and invasion (I) assays. The experiment was repeated thrice.

(J) RFP-labeled cells were transfected with siNUP93 or control siRNAs. Forty-eight hours later, extracts were fractionated and fractions subjected to mass spectrometry using LC-MS/MS-based proteomics. Shown are results obtained in one experiment that used triplicates. The nuclear fractions are presented (Student's t test and *Z*-scoring).

(K) Cells (1.2×10^4) were transfected with a plasmid encoding NUP93 or with an empty vector, along with the indicated reporter plasmids. The luciferase reporters contained response elements for the indicated signaling pathways. MYC-e4 contained the respective enhancer. Luciferase activity was determined in biological triplicates 48 h later. Shown are normalized fold stimulation values from three experiments. *, $p \leq 0.05$; **, $p \leq 0.01$; ***, $p \leq 0.001$; ****, $p \leq 0.0001$.

(L) HEK293 cells were transfected using an NUP93 vector, and lysates were analyzed 48 h later. Similarly, cells expressing an inducible allele of NUP93 were untreated or treated with Tet and 24 h later, extracts were analyzed using antibodies.

(M) The METABRIC dataset was divided into high and low NUP93 expressers. Shown are levels of expression of MYC signature genes (Wilcoxon rank-sum p values: 2.2e−16).

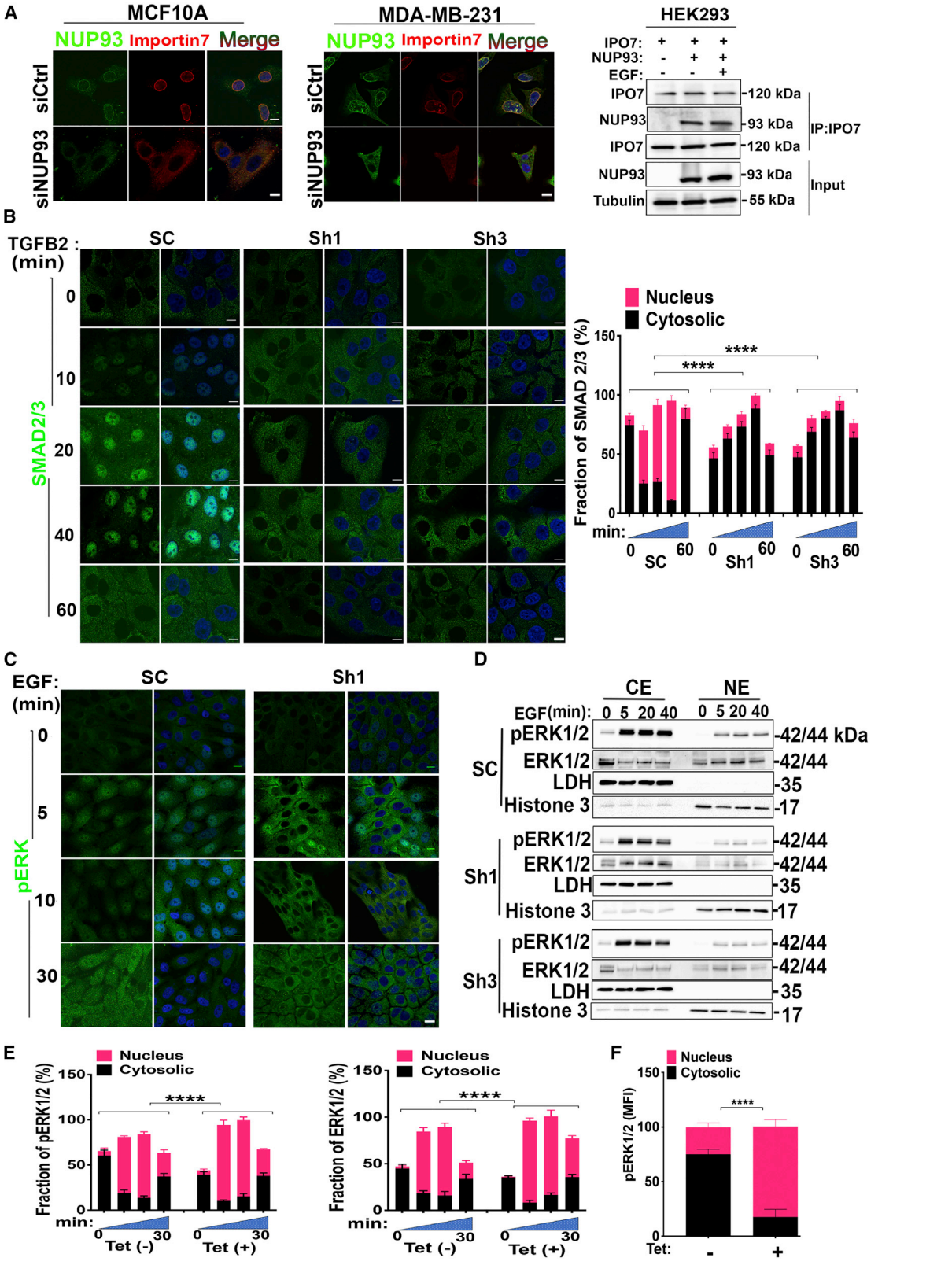

(legend on next page)

high- and low-NUP93 tumors. Next, expression of the previously described MYC gene signature (Zeller et al., 2003) was analyzed in each group. The results reflected significantly increased expression of MYC target genes in the NUP93-high group (Figure 5M), consistent with MYC activation, downstream of overexpressed NUP93, in human mammary tumors.

Multiple RNA transcripts might serve as mediators of the overexpressed NUP93

Along with transport of proteins, the NPC mediates selective nucleocytoplasmic transport of RNA molecules (Sloan et al., 2016). To begin exploring RNA transport, we depleted NUP93 in MCF7 breast cancer cells and examined subcellular localization of polyadenylated transcripts (Figure S5J), as described by Zuckerman et al. (2020). NUP93 depletion led to extensive redistribution of RNA molecules: a statistically significant 3-fold increase in cytoplasmic enrichment of 200 different transcripts and, conversely, a 3-fold increase in nuclear enrichment of transcripts from 153 other genes (Data S3). Because NORAD (a long intergenic non-coding RNA) was detected also by RNA-seq (Figure 3C) and can control metastasis (Yang et al., 2019), we explored NORAD's subcellular distribution using fluorescence *in situ* hybridization. As expected, upon NUP93 depletion, NORAD exhibited strong nuclear enrichment in both MCF7 and MDA-MB-231 cells (Figure S5K). Conceivably, nuclear retention disables NORAD, along with other RNAs and thereby inhibits metastasis of NUP93-low breast cancers. In conclusion, the results indicate that NUP93 acts as a rate-limiting component of the NPC; in addition to selective transport of RNA molecules, overexpression of this nucleoporin permits translocation of β-catenin to the nucleus, thereby activating MYC.

By forming physical complexes with importins, NUP93 accelerates nuclear translocation of ligand-activated transcription factors

The steroid-resistant nephrotic syndrome is caused by *NUP93* mutations, which interfere with ligand-induced SMAD signaling (Braun et al., 2016). Consistent with this, it was shown that insect NUP93 is essential for nuclear import of SMAD (Chen and Xu, 2010). Probing endogenous Importin7 and NUP93 revealed a perinuclear ring of Importin7, overlapping the pattern of NUP93 (Figure 6A, left and middle). Two lines of evidence supported the possibility that cargo-loaded Importin7 molecules dock at NPCs by binding with NUP93: Importin7's perinuclear localization was lost in cells pre-treated with siNUP93, and co-immunoprecipitation analyses detected non-covalent Importin7-NUP93 complexes (Figure 6A, right). Because these complexes were unaffected following treatment with EGF, we assume that NUP93-importin complexes are constitutive, unlike the activation-dependent loading of Importin7 with active SMADs (Chen and Xu, 2010) and ERK (Chuderland et al., 2008).

To test the "cargo-Importin7-NUP93" model, we depleted NUP93 in MCF10A cells and followed nuclear import of SMAD2/3 following treatment with TGF-β2 (Figure 6B). While SMAD2/3 translocated to the nucleus of control cells within 20 min, we observed only limited translocation in NUP93-depleted cells. As an independent line of evidence, we addressed ERK transport using interspecies heterokaryon assays, which apply fusion between donor and recipient cells from two different species (see STAR Methods). Accordingly, human HeLa cells overexpressing NUP93 and ERK2-GFP were fused with murine NIH3T3 fibroblasts that were pre-treated with siNUP93. One day after transfection, co-cultured cells were fused by making use of polyethylene glycol. Quantification of ERK2-GFP fluorescence indicated that siNUP93 reduced the signals we recorded in the nuclei of recipient murine cells (Figure S6A), which lent further support to the ability of NUP93 to enhance the transfer of ERK to the nucleus.

Next, we selectively followed the ligand-activated form of ERK, pERK. Following stimulation with EGF, ERK undergoes phosphorylation that exposes an NTS, which facilitates binding to Importin7 (Chuderland et al., 2008). Accordingly, we detected nuclear translocation of pERK in naive EGF-treated cells, but depletion of NUP93 inhibited pERK translocation (Figure 6C). This difference was verified by means of subcellular fractionation (Figure 6D). Furthermore, we observed reciprocal changes in NUP93-overexpressing cells (Figure 6E). Hence, the next step addressed *in vivo* relevance: we firstly implanted in mice RFP-labeled MDA-MB-231 cells expressing a Tet-inducible allele of NUP93. Once tumors and metastases emerged, we induced NUP93 overexpression for 2 weeks. Probing tumor sections for pERK confirmed significant enrichment for nuclear pERK in Tet-treated lesions (Figure 6F). In summary, both *in vivo* and *in vitro* evidence implied that NUP93 assists translocation of Importin7 molecules loaded with cargoes such as ERK and SMAD.

Figure 6. NUP93 binds with Importin7, and its knockdown inhibits and overexpression enhances nuclear translocation of SMAD and ERK

(A) Left and middle: confocal microscopy of cells transfected with the indicated siRNAs and probed for Importin7 and NUP93. Scale bars, 10 μm. Right: HEK293 T cells (8×10^6) were co-transfected with Importin7 and NUP93 plasmids. EGF treatment (10 ng/mL; 7 min) was applied, 48 h later, on one plate. Cleared extracts were directly resolved or subjected to immunoprecipitation (IP) prior to immunoblotting (IB). The experiments were repeated at least twice. Scale bar, 10 μm.

(B and C) MCF10A cells expressing shNUP93, or control shRNA (SC), were stimulated with TGFB2 (B) or EGF (C). Fixed cells were stained for SMAD2/3 or pERK1/2. Shown are confocal images and quantifications of translocation that were performed in triplicates (averages ± SEM). The experiment was repeated twice. Scale bars, 10 μm.

(D) MCF10A cells pre-stimulated with EGF, as in (C), were fractionated. Lactate dehydrogenase and histone-3 were used as markers. CE and NE, cytoplasmic and nuclear extracts. The experiment was repeated thrice.

(E) MCF10A cells inducibly overexpressing NUP93 were induced and stimulated with EGF. Fixed cells were probed for pERK1/2 (left) and total ERK1/2 (right). The histograms show quantification of protein localization (means of triplicates ± SEM). The experiment was repeated twice.

(F) MDA-MB-231 cells overexpressing a Tet-inducible NUP93 were injected into the fat pad of NOG female mice. Metastasis to lungs was confirmed 15 days later. Thereafter, tetracycline was added to the drinking water and mice were sacrificed 2 weeks later. Deparaffinized lung slices were probed for pERK1/2. Mean fluorescence intensity (MFI) was calculated from eight areas of each slide. The experiment was repeated twice.

****$p \leq 0.0001$ in (B), (E), and (F).

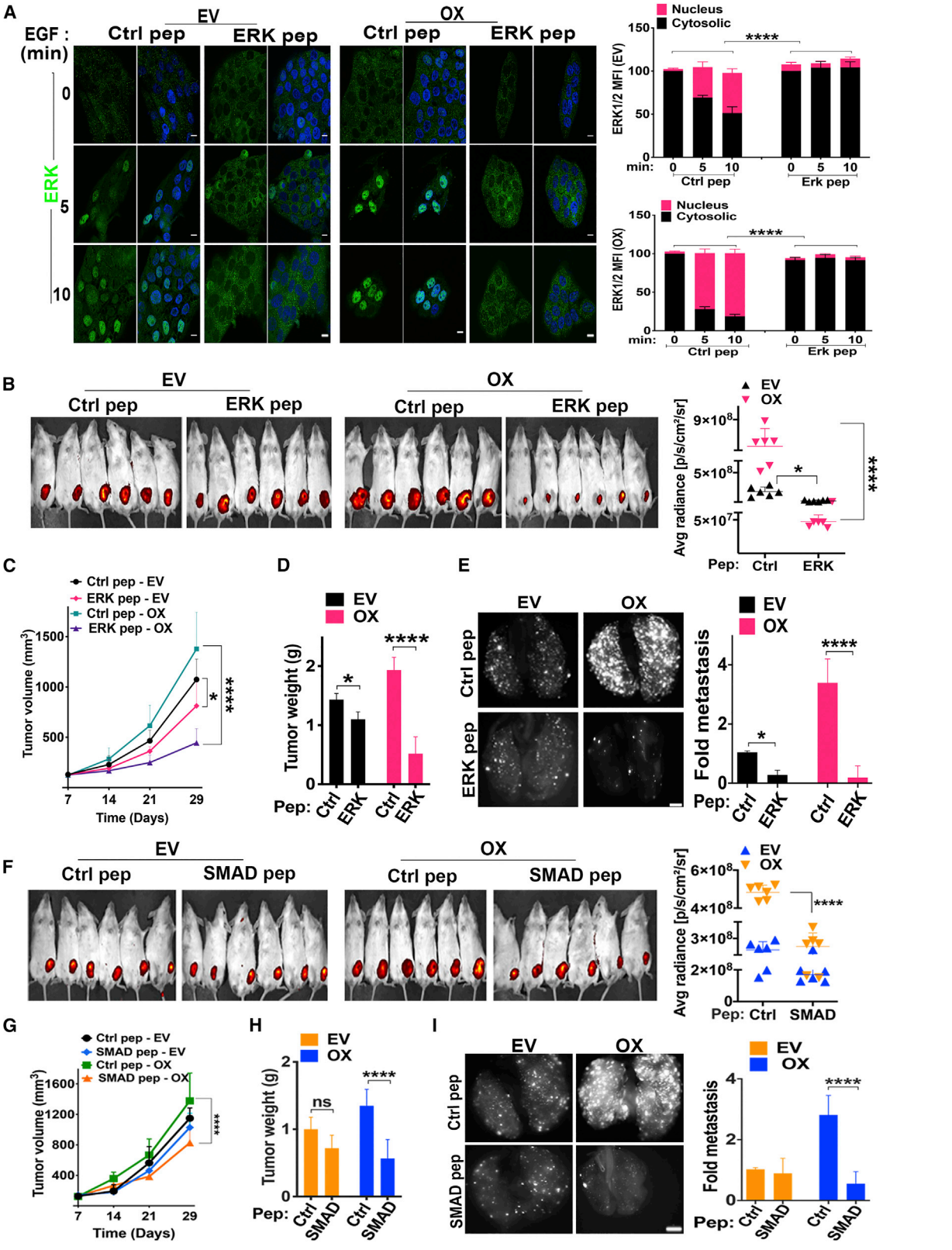

(legend on next page)

In similarity to ERK and SMAD, STAT3 undergoes phosphorylation and nuclear translocation upon stimulation, but α-importins, rather than Importin7, have been implicated (Ushijima et al., 2005). Nevertheless, analyses of both total (Figure S6B) and phosphor STAT3 (Figure S6C) indicated that NUP93 can enhance EGF-induced import of STAT3. These observations implied that NUP93 anchors importins other than Importin7. Hence, we followed two additional cargoes, the glucocorticoid receptor (GR), which is regulated by importin-α/β (Freedman and Yamamoto, 2004), and the p105 subunit of the nuclear factor κB (NF-κB), which is translocated by importins α3 and α4 (Fagerlund et al., 2005). Using NUP93-depleted cells, we observed strong inhibition of GR translocation following stimulation with dexamethasone (DEX), as well as reduced translocation of NF-κB following treatment with the tumor necrosis factor α (see Figures S6D and S6E). In conclusion, NUP93 emerged from these studies as a broad-spectrum transporter of several ligand-stimulated forms of signaling proteins.

Myristoylated peptides corresponding to the NTS of ERK and SMAD inhibit progression of NUP93-overexpressing tumors

Next, we attempted blocking nuclear translocation of ERK and SMAD by preventing binding to Importin7. Our strategy used a previously described membrane-permeable NTS-derived peptide fused to myristic acid (Plotnikov et al., 2015). As expected, the ERK-derived peptide inhibited nuclear accumulation of ERK while a control peptide was inactive (Figure 7A). In addition, the peptide reduced incorporation of radioactive thymidine into DNA only in cells overexpressing NUP93 (Figure S7A). Similar effects were observed with an SMAD-specific peptide (Figure S7B). Likewise, the S-phase fraction observed in cells treated with the ERK peptide was severely reduced (Figure S7C), and the peptide also inhibited the ability of cells to form colonies, migrate, and invade (Figures S7D–S7F). Hence, we implanted NUP93-overexpressing cells in the subaxillary mammary fat pad of mice and, once tumors became palpable, intravenously treated the animals with the ERK peptide. RFP fluorescence and size of the primary tumors were measured (Figures 7B and 7C), along with the final tumor weight (Figure 7D) and lung metastases (Figure 7E). Evidently, tumors overexpressing NUP93 grew faster and colonized lungs better than control tumors. Accordingly, the NUP93-overexpressing tumors and their metastases were more strongly inhibited by the ERK peptide as compared with the control peptide. Interestingly, the ERK peptide weakly, but significantly, inhibited tumors and metastases formed by control MDA-MB-231 cells, implying that NUP93 overexpression confers targetable vulnerability.

Because familial NUP93 mutations causing SRNS displayed defective SMAD signaling (Braun et al., 2016), we made use of an SMAD peptide containing the previously identified Ser-Pro-Ser triad (Chuderland et al., 2008). In addition to nearly complete inhibition of TGF-β-induced nuclear import of SMAD2/3 (Figure S7G), the peptide reduced incorporation of radioactive thymidine (Figure S7B), lowered the S-phase fraction (Figure S7C), and inhibited colony formation, migration, and invasion (Figures S7D–S7F). Next, we implanted NUP93-overexpressing cells in the fat pad of mice and delivered the SMAD peptide thrice per week. RFP fluorescence, as well as tumor volumes (Figures 7F and 7G) and weights (Figure 7H) were determined, and lung metastases were counted (Figure 7I). Whereas the control peptide displayed only weak inhibition of NUP93-overexpressing tumors, significantly stronger effects were observed when treating the overexpressing tumors with the SMAD peptide. Moreover, treatment with the SMAD peptide only weakly inhibited metastasis of control tumors, but the numbers of metastases formed by NUP93-overexpressing cells were reduced by 75%–85%, in line with vulnerability of NUP93 overexpressers. In similarity, it has been reported that inhibition of NPC formation causes cancer cell death while normal cells undergo reversible cell-cycle arrest (Sakuma et al., 2020). Hence, this recent report and our own results exemplify the therapeutic opportunity offered by targeting NUP93.

In summary, the multi-omics platform we established uncovered a group of patients with breast tumors who are characterized by NUP93 overexpression and relatively poor prognosis. Through inducible GOF and LOF strategies, as well as by functionally characterizing two sets of naturally occurring mutants, we demonstrated that NUP93 overexpression can enhance tumor growth and augment metastasis in animal models. Conceivably, by means of physical engagement of importins, the overexpressed NUP93 boosts the final nuclear transport step shared by diverse extracellular cues, especially the WNT/β-catenin pathway, which culminates in MYC activation. As demonstrated here, the previously unknown pathway is targetable in animal models treated with specific membrane-permeable peptides. In aggregate, these lines of evidence identify NUP93 as a driver of tumor growth and metastasis, which hijacks the canonical β-catenin pathway and additional key routes.

DISCUSSION

The results presented here identify NUP93 as a potent driver of growth and metastasis in aggressive subtypes of breast cancer. Unlike other subtypes, the group overexpressing HER2, a

Figure 7. Myristoylated phosphomimetic peptides block nuclear translocation of ERK and SMAD and inhibit progression of NUP93-overexpressing tumors

(A) MCF10A cells overexpressing NUP93 (OX) were treated with the ERK peptide (20 μM; 4 h) or a control peptide (20 μM), then stimulated with EGF. Thereafter, cells were fixed and stained for ERK. Quantitative estimates of nuclear translocation are shown (averages of triplicates ± SEM). Data are representative of three experiments. EV, empty vector; MFI, mean fluorescence intensity. Scale bars, 10 μm.

(B–E) NUP93 overexpressing MDA-MB-231 cells (2×10^6) were inoculated in the mammary fat pad of NOG mice (six mice per group). Once tumor size reached 100 mm^3, mice were intravenously treated with the indicated peptides (30 mg/kg), once every other day. RFP fluorescence (B) and tumor volumes (C) are shown. Tumors weights were determined (D) and lungs were evaluated for metastases (E). The experiment was repeated twice. Scale bar, 0.5 cm.

(F–I) Mice were intravenously treated as in (B), with either the SMAD or the control peptide (30 mg/kg). Primary tumor RFP fluorescence was measured using an *in vivo* optical imaging system. Shown are average tumor volumes (G) and mean final weights (H) from six mice per group. In addition, lungs were evaluated for metastases (I). The data are presented as average numbers of micrometastases ± SEM. The experiment was repeated twice. Scale bar, 0.5 cm.

*$p \leq 0.05$, **$p \leq 0.01$, ****$p \leq 0.0001$.

functional partner of EGFR, is driven by signals mimicking cellular stimulation by growth factors, whereas a fraction of the basal subtype is propelled either by an overexpressed EGFR or by specific downstream mutations (Foulkes et al., 2010). In analogy, our results indicate that the aberrantly overexpressed NUP93 simultaneously amplifies several growth factor signals by means of activating the ultimate nuclear transport step shared by the majority of signal transduction pathways. This entails nuclear translocation of transcription co-activators, such as β-catenin, ERK, SMAD, and STAT. Consistent with this scenario, two bioinformatic lines of evidence identified NUP93 as a putative driver of breast cancer: the first analyzed recurrent CNAs (Tran et al., 2011) while the other addressed driver mutations (Lee et al., 2016). The *in vivo* studies we performed assigned metastasis driver roles to two of the mutant forms, as well as uncovered their ability to enhance basal and ligand-induced nuclear translocation of β-catenin, a well-characterized driver of metastasis.

The analyses we performed offer the following model. Cargo-loaded Importin7 and additional importins dock at NUP93 of nuclear pores and thus gain accessibility to specific DNA REs. Because the tumor microenvironment of mammary cancers constantly supplies growth factors, this presumed mechanism permits cells overexpressing NUP93 to acquire enhanced responses to nearby stromal cells, such as tumor-associated fibroblasts. For these reasons, cancer cells overexpressing NUP93 might become rapidly proliferating and highly metastatic. This model can explain how SMAD proteins, which are escorted by Importin7/8, enhance TGF-β signaling (Xiao et al., 2003), as well as how signals mediated by GR and ERK, two cargoes of Importin7, are augmented when NUP93 is overexpressed. Notably, nuclear translocations of proteins such as β-catenin and NF-κB likely involve importins other than Importin7. For example, a recent genome-wide screen identified Importin11 as a factor required for β-catenin transport (Mis et al., 2020). Regardless of the exact mechanisms enabling NUP93 to control β-catenin import, our promoter-reporter assays indicated that NUP93 strongly regulates the β-catenin pathway and the downstream activation of MYC. This superiority of the LEF1/TCF promoter might be due to two mechanisms, which are not mutually exclusive. The first involves the recently discovered ability of NUP93 to drive expression of cell identity and other genes through interactions with super-enhancers (Bersini et al., 2020; Ibarra et al., 2007). The other mechanism might relate to the rich crosstalk between the WNT pathway and other signaling routes. For example, SMAD3 co-localizes with LEF1 at WNT-responsive elements (Aloysius et al., 2018), and EGFR can transactivate the β-catenin pathway (Yang et al., 2011).

In conclusion, the integrative computational platform we developed has assigned NUP93 with important roles in progression of mammary cancer, which we confirmed in animal models. Remarkably, mammary cells overexpressing NUP93 display overactivation of several growth factor pathways, including the WNT/β-catenin/MYC pathway. This route has repeatedly been associated with colorectal tumors, but recent network-based analysis linked it also to breast cancer (Koval and Katanaev, 2018). Thus, by seizing an essential step common to multiple signaling routes, NUP93 has acquired robust oncogenic attributes. Beyond the identification of augmented nuclear transport as a previously unappreciated hallmark of cancer, our study offers a target for intervention as well as a pharmacological strategy tailored to the subset of patients whose tumors overexpress NUP93.

Limitations of the study

The stoichiometry of the NPC might be a limitation of our study. In other words, our results do not explain how overexpression of a single component of the NPC, which comprises >30 other distinct proteins, increases nucleocytoplasmic transport. Possibly, NUP93 acts as a nucleation center that attracts soluble components to newly formed NPCs, but this has not been addressed. Another potential caveat is the possibility that NUP93 overexpression boosts export of proteins, including ribosome subunits, to the cytoplasm. Presumably, such export events are synchronized with the cell cycle in malignant cells, but we have not addressed this model. Yet a third limitation of the study relates to potential interactions of NUP93 with the chromatin of breast cancer cells, especially enhancer elements, which were not analyzed by our experiments.

STAR★METHODS

Detailed methods are provided in the online version of this paper and include the following:

- KEY RESOURCES TABLE
- RESOURCE AVAILABILITY
  - Lead contact
  - Materials availability
  - Data and code availability
- EXPERIMENTAL MODEL AND SUBJECT DETAILS
  - Cell lines
  - Mice
- METHOD DETAILS
  - Lentivirus construct and RNA interference
  - Immunoblotting and immunoprecipitation analyses
  - Nuclear and cytoplasmic fractionation
  - Thymidine incorporation assays
  - Cell cycle analysis and ImageStream analyses
  - Determination of receptor expression levels
  - Cell proliferation assays
  - Cell migration, invasion, and 3D assays
  - Clonogenic growth assay and adhesion assays
  - Immunofluorescence and live image analyses
  - Immunofluorescence analyses
  - Electron microscopy
  - Inter-species heterokaryon assays
  - Synthetic myristoylated peptides
  - Immunohistochemistry and picrosirius red staining
  - Invadopodia assays
  - Rho GTPase activation assays and ELISA tests
  - Luciferase-reporter assays
  - RNA isolation, real-time PCR analysis and RNA sequencing
  - Extraction and sequencing of cytoplasmic and nuclear RNA

- Single molecule FISH
- *In vitro* knockout of the gene encoding for NUP93
- Proteomic analysis

- QUANTIFICATION AND STATISTICAL ANALYSIS

SUPPLEMENTAL INFORMATION

Supplemental information can be found online at https://doi.org/10.1016/j.celrep.2022.110418.

ACKNOWLEDGMENTS

We thank Drs. Friedhelm Hildebrandt, Robert Weinberg, Jeffrey Wrana, Daniel Haber, Stefan Wiemann, and Tohru Itoh for plasmids and Dr. Raya Eilam-Altstadter for histology analyses. This work was performed in the Marvin Tanner Laboratory for Research on Cancer. Y.Y. is the incumbent of the Harold and Zelda Goldenberg Professorial Chair in Molecular Cell Biology. Our studies have been supported by the Israel Science Foundation (ISF), the Israel Cancer Research Fund (ICRF), the European Research Council (ERC), and the Dr. Miriam and Sheldon G. Adelson Medical Research Foundation (AMRF).

AUTHOR CONTRIBUTIONS

N.B.N. and Y.Y. designed experiments and wrote the manuscript; N.B.N., A.N., S.G., H.R.M.R., A.S., B.Z., M.L., E.T., S.S., M.S., and I.L. performed experiments and analyzed the results; J.S.L., D.D.-G., and O.R. performed bioinformatic analyses; and C.C., S.L., T.G., A.C., I.U., R.S., and E.R. supervised research, analyzed results, and reviewed the manuscript.

DECLARATION OF INTERESTS

The authors declare no competing interests.

Received: March 11, 2021
Revised: October 14, 2021
Accepted: February 1, 2022
Published: February 22, 2022

REFERENCES

Aloysius, A., DasGupta, R., and Dhawan, J. (2018). The transcription factor Lef1 switches partners from beta-catenin to Smad3 during muscle stem cell quiescence. Sci. Signal *11*, eaan3000.

Anders, S., Pyl, P.T., and Huber, W. (2015). HTSeq–a Python framework to work with high-throughput sequencing data. Bioinformatics *31*, 166–169.

Bartholin, L., Wessner, L.L., Chirgwin, J.M., and Guise, T.A. (2007). The human Cyr61 gene is a transcriptional target of transforming growth factor beta in cancer cells. Cancer Lett. *246*, 230–236.

Baselga, J., and Swain, S.M. (2010). CLEOPATRA: a phase III evaluation of pertuzumab and trastuzumab for HER2-positive metastatic breast cancer. Clin. Breast Cancer *10*, 489–491.

Benjamini, Y., and Hochberg, Y. (1995). Controlling the false discovery rate: a practical and powerful approach to multiple testing. J. R. Stat. Soc. Ser. B (Methodological) *57*, 289–300.

Bersini, S., Lytle, N.K., Schulte, R., Huang, L., Wahl, G.M., and Hetzer, M.W. (2020). Nup93 regulates breast tumor growth by modulating cell proliferation and actin cytoskeleton remodeling. Life Sci. Alliance *3*, 1–15.

Braun, D.A., Sadowski, C.E., Kohl, S., Lovric, S., Astrinidis, S.A., Pabst, W.L., Gee, H.Y., Ashraf, S., Lawson, J.A., Shril, S., et al. (2016). Mutations in nuclear pore genes NUP93, NUP205 and XPO5 cause steroid-resistant nephrotic syndrome. Nat. Genet. *48*, 457–465.

Chen, S.J., Ning, H., Ishida, W., Sodin-Semrl, S., Takagawa, S., Mori, Y., and Varga, J. (2006). The early-immediate gene EGR-1 is induced by transforming growth factor-beta and mediates stimulation of collagen gene expression. J. Biol. Chem. *281*, 21183–21197.

Chen, X., and Xu, L. (2010). Specific nucleoporin requirement for Smad nuclear translocation. Mol. Cell Biol. *30*, 4022–4034.

Cheung, H.W., Cowley, G.S., Weir, B.A., Boehm, J.S., Rusin, S., Scott, J.A., East, A., Ali, L.D., Lizotte, P.H., Wong, T.C., et al. (2011). Systematic investigation of genetic vulnerabilities across cancer cell lines reveals lineage-specific dependencies in ovarian cancer. Proc. Natl. Acad. Sci. U S A *108*, 12372–12377.

Chuderland, D., Konson, A., and Seger, R. (2008). Identification and characterization of a general nuclear translocation signal in signaling proteins. Mol. Cell *31*, 850–861.

Cox, J., Neuhauser, N., Michalski, A., Scheltema, R.A., Olsen, J.V., and Mann, M. (2011). Andromeda: a peptide search engine integrated into the MaxQuant environment. J. Proteome Res. *10*, 1794–1805.

Curtis, C., Shah, S.P., Chin, S.F., Turashvili, G., Rueda, O.M., Dunning, M.J., Speed, D., Lynch, A.G., Samarajiwa, S., Yuan, Y., et al. (2012). The genomic and transcriptomic architecture of 2,000 breast tumours reveals novel subgroups. Nature *486*, 346–352.

Dawson, S.J., Rueda, O.M., Aparicio, S., and Caldas, C. (2013). A new genome-driven integrated classification of breast cancer and its implications. EMBO J. *32*, 617–628.

Dobin, A., Davis, C.A., Schlesinger, F., Drenkow, J., Zaleski, C., Jha, S., Batut, P., Chaisson, M., and Gingeras, T.R. (2013). STAR: ultrafast universal RNA-seq aligner. Bioinformatics *29*, 15–21.

Fagerlund, R., Kinnunen, L., Kohler, M., Julkunen, I., and Melen, K. (2005). NF-{kappa}B is transported into the nucleus by importin {alpha}3 and importin {alpha}4. J. Biol. Chem. *280*, 15942–15951.

Foulkes, W.D., Smith, I.E., and Reis-Filho, J.S. (2010). Triple-negative breast cancer. N. Engl. J. Med. *363*, 1938–1948.

Freedman, N.D., and Yamamoto, K.R. (2004). Importin 7 and importin alpha/importin beta are nuclear import receptors for the glucocorticoid receptor. Mol. Biol. Cell *15*, 2276–2286.

Herbst, A., Jurinovic, V., Krebs, S., Thieme, S.E., Blum, H., Goke, B., and Kolligs, F.T. (2014). Comprehensive analysis of beta-catenin target genes in colorectal carcinoma cell lines with deregulated Wnt/beta-catenin signaling. BMC Genomics *15*, 74.

Hughes, C.S., Moggridge, S., Muller, T., Sorensen, P.H., Morin, G.B., and Krijgsveld, J. (2019). Single-pot, solid-phase-enhanced sample preparation for proteomics experiments. Nat. Protoc. *14*, 68–85.

Hynes, R.O., and Naba, A. (2012). Overview of the matrisome–an inventory of extracellular matrix constituents and functions. Cold Spring Harb. Perspect. Biol. *4*, a004903.

Ibarra, I., Erlich, Y., Muthuswamy, S.K., Sachidanandam, R., and Hannon, G.J. (2007). A role for microRNAs in maintenance of mouse mammary epithelial progenitor cells. Genes Dev. *21*, 3238–3243.

Itahana, Y., Yeh, E.T., and Zhang, Y. (2006). Nucleocytoplasmic shuttling modulates activity and ubiquitination-dependent turnover of SUMO-specific protease 2. Mol. Cell Biol *26*, 4675–4689.

Jin, L., Pahuja, K.B., Wickliffe, K.E., Gorur, A., Baumgartel, C., Schekman, R., and Rape, M. (2012). Ubiquitin-dependent regulation of COPII coat size and function. Nature *482*, 495–500.

Kanojia, D., Morshed, R.A., Zhang, L., Miska, J.M., Qiao, J., Kim, J.W., Pytel, P., Balyasnikova, I.V., Lesniak, M.S., and Ahmed, A.U. (2015). betaIII-tubulin regulates breast cancer metastases to the brain. Mol. Cancer Ther. *14*, 1152–1161.

Knockenhauer, K.E., and Schwartz, T.U. (2016). The nuclear pore complex as a flexible and dynamic gate. Cell *164*, 1162–1171.

Koval, A., and Katanaev, V.L. (2018). Dramatic dysbalancing of the Wnt pathway in breast cancers. Sci. Rep. *8*, 7329.

Lalanne, J.B., Taggart, J.C., Guo, M.S., Herzel, L., Schieler, A., and Li, G.W. (2018). Evolutionary convergence of pathway-specific enzyme expression stoichiometry. Cell *173*, 749–761 e738.

Lee, J.H., Zhao, X.M., Yoon, I., Lee, J.Y., Kwon, N.H., Wang, Y.Y., Lee, K.M., Lee, M.J., Kim, J., Moon, H.G., et al. (2016). Integrative analysis of mutational and transcriptional profiles reveals driver mutations of metastatic breast cancers. Cell Discov *2*, 16025.

Li, B., and Dewey, C.N. (2011). RSEM: accurate transcript quantification from RNA-Seq data with or without a reference genome. BMC Bioinformatics *12*, 323.

Li, L., Artlett, C.M., Jimenez, S.A., Hall, D.J., and Varga, J. (1995). Positive regulation of human alpha 1 (I) collagen promoter activity by transcription factor Sp1. Gene *164*, 229–234.

Love, M.I., Huber, W., and Anders, S. (2014). Moderated estimation of fold change and dispersion for RNA-seq data with DESeq2. Genome Biol. *15*, 550.

Maik-Rachline, G., Hacohen-Lev-Ran, A., and Seger, R. (2019). Nuclear ERK: mechanism of translocation, substrates, and role in cancer. Int. J. Mol. Sci. *20*, 1194.

McQuin, C., Goodman, A., Chernyshev, V., Kamentsky, L., Cimini, B.A., Karhohs, K.W., Doan, M., Ding, L., Rafelski, S.M., Thirstrup, D., et al. (2018). CellProfiler 3.0: next-generation image processing for biology. PLoS Biol. *16*, e2005970.

Mis, M., O'Brien, S., Steinhart, Z., Lin, S., Hart, T., Moffat, J., and Angers, S. (2020). IPO11 mediates betacatenin nuclear import in a subset of colorectal cancers. J. Cell Biol *219*, 1–13.

Mueller, F., Senecal, A., Tantale, K., Marie-Nelly, H., Ly, N., Collin, O., Basyuk, E., Bertrand, E., Darzacq, X., and Zimmer, C. (2013). FISH-quant: automatic counting of transcripts in 3D FISH images. Nat. Methods *10*, 277–278.

Mueller, S., Engleitner, T., Maresch, R., Zukowska, M., Lange, S., Kaltenbacher, T., Konukiewitz, B., Ollinger, R., Zwiebel, M., Strong, A., et al. (2018). Evolutionary routes and KRAS dosage define pancreatic cancer phenotypes. Nature *554*, 62–68.

Nair, N.U., Das, A., Rogkoti, V.-M., Fokkelman, M., Marcotte, R., de Jong, C.G., Koedoot, E., Lee, J.S., Meilijson, I., Hannenhalli, S., et al. (2019). Migration rather than proliferation transcriptomic signatures are strongly associated with breast cancer patient survival. Sci. Rep. *9*, 10989.

Nusse, R., and Clevers, H. (2017). Wnt/beta-Catenin signaling, disease, and emerging therapeutic modalities. Cell *169*, 985–999.

Paterson, E.K., and Courtneidge, S.A. (2018). Invadosomes are coming: new insights into function and disease relevance. FEBS J. *285*, 8–27.

Petropoulos, C., Oddou, C., Emadali, A., Hiriart-Bryant, E., Boyault, C., Faurobert, E., Vande Pol, S., Kim-Kaneyama, J.R., Kraut, A., Coute, Y., et al. (2016). Roles of paxillin family members in adhesion and ECM degradation coupling at invadosomes. J. Cell Biol *213*, 585–599.

Plotnikov, A., Flores, K., Maik-Rachline, G., Zehorai, E., Kapri-Pardes, E., Berti, D.A., Hanoch, T., Besser, M.J., and Seger, R. (2015). The nuclear translocation of ERK1/2 as an anticancer target. Nat. Commun. *6*, 6685.

Ran, F.A., Hsu, P.D., Wright, J., Agarwala, V., Scott, D.A., and Zhang, F. (2013). Genome engineering using the CRISPR-Cas9 system. Nat. Protoc. *8*, 2281–2308.

Sakuma, S., Raices, M., Borlido, J., Guglielmi, V., Zhu, E.Y.S., and D'Angelo, M.A. (2020). Inhibition of nuclear pore complex formation selectively induces cancer cell death. Cancer Discov. *11*, 176–193.

Scholz, B.A., Sumida, N., de Lima, C.D.M., Chachoua, I., Martino, M., Tzelepis, I., Nikoshkov, A., Zhao, H., Mehmood, R., Sifakis, E.G., et al. (2019). WNT signaling and AHCTF1 promote oncogenic MYC expression through super-enhancer-mediated gene gating. Nat Genet *51*, 1723–1731.

Slamon, D.J., Godolphin, W., Jones, L.A., Holt, J.A., Wong, S.G., Keith, D.E., Levin, W.J., Stuart, S.G., Udove, J., Ullrich, A., et al. (1989). Studies of the HER-2/neu proto-oncogene in human breast and ovarian cancer. Science *244*, 707–712.

Sloan, K.E., Gleizes, P.E., and Bohnsack, M.T. (2016). Nucleocytoplasmic transport of RNAs and RNA-protein complexes. J. Mol. Biol. *428*, 2040–2059.

Srivastava, S., Nataraj, N.B., Sekar, A., Ghosh, S., Bornstein, C., Drago-Garcia, D., Roth, L., Romaniello, D., Marrocco, I., David, E., et al. (2019). ETS proteins bind with glucocorticoid receptors: relevance for treatment of ewing sarcoma. Cell Rep. *29*, 104–117.e104.

Suzuki, N., Zara, J., Sato, T., Ong, E., Bakhiet, N., Oshima, R.G., Watson, K.L., and Fukuda, M.N. (1998). A cytoplasmic protein, bystin, interacts with trophinin, tastin, and cytokeratin and may be involved in trophinin-mediated cell adhesion between trophoblast and endometrial epithelial cells. Proc. Natl. Acad. Sci. U S A *95*, 5027–5032.

Tran, L.M., Zhang, B., Zhang, Z., Zhang, C., Xie, T., Lamb, J.R., Dai, H., Schadt, E.E., and Zhu, J. (2011). Inferring causal genomic alterations in breast cancer using gene expression data. BMC Syst. Biol. *5*, 121.

Tyanova, S., Temu, T., Sinitcyn, P., Carlson, A., Hein, M.Y., Geiger, T., Mann, M., and Cox, J. (2016). The Perseus computational platform for comprehensive analysis of (prote)omics data. Nat. Methods *13*, 731–740.

Ushijima, R., Sakaguchi, N., Kano, A., Maruyama, A., Miyamoto, Y., Sekimoto, T., Yoneda, Y., Ogino, K., and Tachibana, T. (2005). Extracellular signal-dependent nuclear import of STAT3 is mediated by various importin alphas. Biochem. Biophys. Res. Commun. *330*, 880–886.

Xiao, Z., Latek, R., and Lodish, H.F. (2003). An extended bipartite nuclear localization signal in Smad4 is required for its nuclear import and transcriptional activity. Oncogene *22*, 1057–1069.

Yang, W., Xia, Y., Ji, H., Zheng, Y., Liang, J., Huang, W., Gao, X., Aldape, K., and Lu, Z. (2011). Nuclear PKM2 regulates β-catenin transactivation upon EGFR activation. Nature *480*, 118–122.

Yang, Z., Zhao, Y., Lin, G., Zhou, X., Jiang, X., and Zhao, H. (2019). Noncoding RNA activated by DNA damage (NORAD): biologic function and mechanisms in human cancers. Clin. Chim. Acta *489*, 5–9.

Yarden, Y., and Pines, G. (2012). The ERBB network: at last, cancer therapy meets systems biology. Nat. Rev. Cancer *12*, 553–563.

Zeller, K.I., Jegga, A.G., Aronow, B.J., O'Donnell, K.A., and Dang, C.V. (2003). An integrated database of genes responsive to the Myc oncogenic transcription factor: identification of direct genomic targets. Genome Biol. *4*, R69.

Zuckerman, B., Ron, M., Mikl, M., Segal, E., and Ulitsky, I. (2020). Gene architecture and sequence composition underpin selective dependency of nuclear export of long RNAs on NXF1 and the TREX complex. Mol. Cell *79*, 251–267 e256.

Zuo, Y., Oh, W., Ulu, A., and Frost, J.A. (2016). Minireview: mouse models of Rho GTPase function in mammary gland development, tumorigenesis, and metastasis. Mol. Endocrinol. *30*, 278–289.

STAR★METHODS

KEY RESOURCES TABLE

REAGENT or RESOURCE	SOURCE	IDENTIFIER
Antibodies		
Mouse monoclonal anti-Brdu	Invitrogen	Cat# 175071
Rabbit polyclonal anti-NUP93	Sigma	Cat# HPA017937
Mouse monoclonal anti-NUP93	Santa Cruz Biotechnology	Cat# SC374399
Mouse monoclonal anti-NUP93	Santa Cruz Biotechnology	Cat# SC374400
Mouse monoclonal anti-GAPDH	Merck	Cat# MAB374
Mouse monoclonal anti-RAS-GAP	Santa Cruz Biotechnology	Cat# SC63
Goat Polyclonal anti-LDH	Santa Cruz Biotechnology	Cat# SC27230
Rabbit polyclonal anti- Histone 3	Abcam	Cat# AB1791
Rabbit monoconal anti-pSTAT3	Cell Signaling Technology	Cat# 9145
Rabbit polyclonal anti-ERK	SantaCruz Biotechnology	Cat# SC154
Goat polyclonal Anti-pERK	Santa Cruz Biotechnology	Cat# SC16982
Mouse monoclonal anti-ERK1/2	Sigma	Cat# M8159
Rat Monoclonal anti- Integrin Alpha 5	Millipore	Cat# MABT822
Rabbit monoclonal anti- Beta Catenin	Cell Signaling Technology	Cat# 8480
Mouse monoclonal anti-integrin beta 1	Millipore	Cat# MAB1965
Rabbit monoclonal anti-SMAD2/3	Cell Signaling Technology	Cat# 5678
Rabbit monoclonal anti-pSMAD2/3	Cell Signaling Technology	Cat# 8827
Goat Polyclonal anti-TGFbeta- R2	R & D systems	Cat# AF241
Rabbit monoclonal IgG Isotype control	Abcam	Cat# Ab172730
Goat polyclonal IgG Control	R & D systems	Cat# Ab108C
Mouse polyclonal IgG control	Abcam	Cat# ab37355
Collagen IV alpha6	Abcam	Cat# ab221554
Mouse IgG1 anti-paxillin	BD Biosciences	Cat# 610052
Mouse IgG1 anti-HIC5	BD Biosciences	Cat# 611164
Rabbit anti-LPP	Immunoglobe, Germany	Cat# 003205
Rabbit polyclonal anti-BYSL	Abcam	Cat# Ab251811
Rabbit monoclonal anti- Beta Catenin	Abcam	Cat# Ab32572
Rabbit polyclonal anti-PODXL	Abcam	Cat # Ab154305
Mouse monoclonal anti- Fascin	Cell Signaling Technology	Cat# 54545
Goat polyclonal anti-IPO7	Novus Biosciences	Cat# NB1001081
moue monoclonal anti- STAT3	Cell Signaling Technology	Cat# 9139
Mouse monoclonal anti-GR	Santa Cruz Biotechnology	Cat# sc-393232
Rabbit polyclonal anti-GR	Santa Cruz Biotechnology	Cat# sc-8992
Rabbit monoclonal anti-ERK	Cell Signaling Technology	Cat# 4695
Rabbit monoclonal anti-pERK	Cell Signaling Technology	Cat# 9101
Rabbit polyclonal anti-culin3	Sigma	Cat# C0871
Rabbit polyclonal- anti SP1	Santa Cruz Biotechnology	Cat# Sc-59
Mouse monoclonal anti-axin	Abcam	Cat# Ab233652
Rabbit polyclonal anti-Importin 7	Abcam	Cat#Ab99273
Chemicals, peptides, and recombinant proteins		
Liquid scintillation cocktail	Perkin Elmer, USA	Cat# 6013329
d-Luciferin	Perkin Elmer, USA	Cat# 122799
3 [H]-thymidine	Perkin Elmer, USA	Cat# NET027Z001MC

(*Continued on next page*)

Continued

REAGENT or RESOURCE	SOURCE	IDENTIFIER
Phalloidin	Sigma-Aldrich	Cat# P1951; P5282
Tetracycline	Sigma	Cat# T7660
Doxycycline	Sigma	Cat# D9891
Fibronectin	Biological Industries	Cat# 05-750-1F
Cyclohexamide	Sigma	Cat# 66-81-8
Picro-sirius red solution	Abcam	Cat# Ab246832
Critical commercial assays		
Transwell	COSTAR	Cat# 3422
Matrigel Invasion Chamber	BD Biosciences	Cat# FAL354480
Genomic Isolation Kit	Invitrogen	Cat# K182001
Midi Prep Kit	Qiagen	Cat# 12143
SYBR Green PCR Master Mix	Thermo Fisher Scientific	Cat# 4309155
High-Capacity cDNA Reverse Transcription Kit	Thermo Fisher Scientific	Cat# 4368814
Dual-Luciferase Reporter Assay System	Promega	Cat# E1910
TGF beta 1 elisa kit	R & D systems	Cat# DY240
TGF beta 2 elisa kit	R & D systems	Cat# DY302
TGF beta RII elisa kit	R & D systems	Cat#DY241
VEGF elisa Kit	R & D systems	Cat# CY293B
TGF beta 2	Peprotech	Cat#100–35B
EGF	Sigma	Cat# E9644
XTT	Biological Industries	Cat# 20-300-1000
Lipofectamine LTX and Plus	Invitrogen	Cat# 15338100
Rho/Rac/cdc42 G-LISA activation kit	Cytoskeleton, Inc	Cat# BK135
3D assay kit	Cultrex	Cat# 3500096K
FluoroBlok	Corning	Cat# 351157
Ras activation kit	Cytoskeleton, Inc	Cat# BK131
Luciferase kit	Promega	Cat# E1910
RNA Isolation kit	5 prime	Cat# 2302350
RNA Isolation kit	Quiagen	Cat# 217004
Deposited data		
RNA sequencing data	This paper	Accession number: GSE156103
Experimental models: Cell lines		
Human:MDA-MB-231	ATCC	Cat# HTB26
Human: HEK293T	ATCC	Cat# CRL-3216
MCF10A	ATCC	Cat# CRL-10317
HUVEC	ATCC	Cat# CRL-1730
MCF7	ATCC	Cat# HTB-22
Experimental models: Organisms/strains		
NOG	Jackson	Cat# 005557
Oligonucleotides		
shNUP93	GE healthcare	Cat# V3SH11243
siNUP93	GE healthcare	Cat# L020767
Inducible shNUP93	GE healthcare	Cat# V3SH11252
siLEF1	Dharmacon	Cat# L015396
siBYSL	Dharmacon	Cat# L011818
siCulin3	Dharmacon	Cat# L010224
siPODXL	Dharmacon	Cat# L010617

(*Continued on next page*)

Continued

REAGENT or RESOURCE	SOURCE	IDENTIFIER
gRNA EXON 5	CAACCAACATTGACTCCCGA	N/A
gRNA EXON 5	CTATAGGTTTGACTGTCCCA	N/A
Recombinant DNA		
pLEX_305	Addgene	Cat# 41390
pLEX_307	Addgene	Cat# 41392
CCSB-NUP93	GE healthcare	Cat# OHS1770
NUP93-pLEX 307	this paper	NA
NUP93- pLenti 6.3/TO	this paper	NA
R327C-pLEX 307	this paper	NA
E14K-pLEX 307	this paper	NA
SpCas9-2A-GFP	Addgene	Cat# 48138
FHRE luciferase	Addgene	Cat #1789
STAT luciferase	Addgene	Cat# 37392
SRE luciferase	Addgene	Cat# 82686
Top Flash luciferase	Addgene	Cat# 12456
SMAD4 luciferase	Qiagen	Cat# CCS-017L
Notch1 luciferase	Qiagen	Cat# CCS-014L
AP1 luciferase	Addgene	Cat# 40342
FOP	Addgene	Cat# 12457
SM FISH Probes (NORAD)	Stellaris	N/A
Collagen 18 luciferase	GeneCopoeia	Customized
Collagen 4 alpha 1	GeneCopoeia	Customized
Software and algorithms		
ImageJ	National Institutes of Health, Bethesda, USA	https://imagej.nih.gov/ij/
Prism 8	Graph pad	https://www.graphpad.com/scientific-software/prism/
BD FACS Diva software v8.0.1	BD Biosciences	https://www.bdbiosciences.com/us/instruments/research/software/flow-cytometry-acquisition/bd-facsdiva-software/m/111112/features
IVIS	Perkin Elmer, USA	https://www.perkinelmer.com/lab-products-and-services/resources/in-vivo-imaging-software-downloads.html#LivingImage
Other		
pCDNA6.2 NGFP- G591V-NUP93	Gift from Dr. Hildebrandt, Harvard Medical School	N/A
pCDNA6.2 NGFP- Y629C-NUP93	Gift from Dr. Hildebrandt, Harvard Medical School	N/A
pRK5 N Myc- NUP93	Gift from Dr. Hildebrandt, Harvard Medical School	N/A
pRK5 C Myc- NUP93	Gift from Dr. Hildebrandt, Harvard Medical School	N/A
pCDNA6.2 N GFP- NUP93	Gift from Dr. Hildebrandt, Harvard Medical School	N/A
pCDNA6.2 C GFP- NUP93	Gift from Dr. Hildebrandt, Harvard Medical School	N/A
GRE-luciferase plasmid	Gift from Prof. Anne Gompel, Paris Descartes University	N/A
FLI1-BS-luciferase plasmid	Gift from Prof. Anne Gompel, Paris Descartes University	N/A

RESOURCE AVAILABILITY

Lead contact

Further information and requests for resources and reagents should be directed to and will be fulfilled by the lead contact, Yosef Yarden (yosef.yarden@weizmann.ac.il).

Materials availability

All materials we generated will be made available upon request. The sources and identifiers of all materials are listed in the key resources table.

Data and code availability

- RNA-seq data have been deposited at GEO and are publicly available. Accession numbers are listed in the key resources table.
- This paper reports no original code.
- Any additional information required to reanalyze the data reported in this paper is available from the lead contact upon request.

EXPERIMENTAL MODEL AND SUBJECT DETAILS

Cell lines

HeLa, HEK293 and NIH-3T3 cells were cultured in Dulbecco's modified Eagle's medium containing fetal bovine serum (10%; FBS). WNT-3A producing L cells and control L cells were cultured according to ATCC manual. MCF10A cells were grown in DME/F12 (1:1) supplemented with antibiotics, insulin (0.01 mg/mL), cholera toxin (0.1 μg/mL), hydrocortisone (0.5 μg/mL), heat-inactivated horse serum (5%, v/v), and EGF (10 ng/mL). Human mammary MDA-MB-231 and MCF7 cells were grown in RPMI-1640 medium (Gibco BRL) supplemented with 10% heat inactivated FBS (Gibco), 1 mM sodium pyruvate, and a penicillin streptomycin mixture (100 U/mL; 0.1 mg/mL). HUVEC cells were cultured in EGM as per the optimized protocol of Lonza. Stable MDA-MB-231-RFP-LUC clones were generated using electroporation and the NEPA gene electroporator.

Mice

All *in vivo* studies were reviewed and approved by the Weizmann Institute's Animal Care and Use Committee (IACUC). Six-weeks old NOG/NSG female mice (Jackson Laboratories) were bred at the Animal Resources Center at the Weizmann Institute. Six mice per group were used in all experiments. Mice were housed in a specific pathogen-free environment. Only female 6–7 weeks old mice were used in this study. Mice were maintained with a 12 h light/dark cycle and they were fed standard chow. MDA-MB-231-RFP-LUC cells were implanted in the fat pad or tail vein, as indicated in the legends to figures. Tumor sizes were calculated according to the following formula: $V = (4\pi/3) \times (\alpha/2)^2 \times (b/2)$. Metastases in different organs were visualized using a fluorescent binocular microscope or IVIS (Xenogen Corp.).

METHOD DETAILS

Lentivirus construct and RNA interference

Nontargeted shRNAs (control) and shRNAs directed against human NUP93 were produced in human embryonic kidney (HEK) 293 cells following the manufacturer's guidelines (GE Healthcare). Target cells were infected with shRNA-encoding lentiviruses supplemented with polybrene (8 μg/mL) and cultured in the presence of puromycin (2 μg/mL) for 4 days. Stable gene expression was achieved using the ViraPower lentiviral expression system (Invitrogen) following the manufacturer's guidelines. siRNA oligonucleotides were purchased from Dharmacon. For knockdown experiments, cells were seeded in 6-well plates at 50% confluence, and 24 h later, they were transfected with siRNA SMART pools using the Lipofectamine 2000 transfection reagent (Life Technologies).

Immunoblotting and immunoprecipitation analyses

Cells were washed briefly with ice-cold saline and scraped in a buffered detergent solution (25 mM Hepes (pH 7.5), 150 mM NaCl, 0.5% Na-deoxycholate, 1% NP-40, 0.1% SDS, 1 mM EDTA, 1 mM EGTA, 0.2 mM Na_3VO_4, and a protease inhibitor cocktail). For equal gel loading, protein concentrations were determined using the bicinchoninic acid (Pierce) reagent. Co-immunoprecipitation assays used protein A beads or anti-GFP beads. Following gel electrophoresis, proteins were transferred onto a nitrocellulose membrane. The membrane was blocked in TBST buffer (0.02 M tris-HCl (pH 7.5), 0.15 M NaCl, and 0.05% Tween 20) containing albumin (3%), blotted with a primary antibody (at 4°C), washed in TBST and incubated for 30 min with a secondary antibody conjugated to horseradish peroxidase.

Nuclear and cytoplasmic fractionation

Cell pellets were lysed in 0.1 mL cytoplasmic lysis buffer (10 mM HEPES pH 7.9, 10 mM KCl, 0.1 mM EGTA, 0.1 mM EDTA, 1 mM DTT and 0.5% NP-40). The cytoplasmic fraction was collected using centrifugation (600Xg for 5 min). Nuclei were washed and resus-

pended in nuclear lysis buffer (50 mL; 20 mM HEPES pH 7.9, 0.4 M NaCl, 1 mM EGTA, 1 mM EDTA, 1 mM DTT) by repeated freezing and thawing. Supernatants containing the nuclear fraction were collected by means of centrifugation at 12,000 rpm for 20 min.

Thymidine incorporation assays

Cells were plated onto 24-well plates, and 16 h later the medium was replaced with fresh medium containing ^{3}H-thymidine (1 μCi). At the indicated time points, the incubation was terminated by the addition of ice-cold trichloroacetic acid (5%; TCA). Five minutes later, cells were solubilized at 37°C with NaOH (1N; for 10 min) followed by HCL (1N). Samples were collected into scintillation vials. Radioactivity was determined in a scintillation counter.

Cell cycle analysis and ImageStream analyses

Cells were incubated for 60 min with bromodeoxyuridine (BrdU; 10 μM) and then washed, harvested and fixed in ethanol (at 4°C). Thereafter, cells were incubated in a denaturation solution (2N HCl, 0.5% Triton-X100; 30 min), followed by a neutralization solution (0.1 M sodium borate, pH 8.5; 30 min). BrdU incorporated into newly synthetized DNA was assayed using an APC-conjugated anti-BrdU antibody. Total DNA content was determined using a propidium iodide solution supplemented with RNase A. Cell cycle distribution was detected by flow cytometry. Further analysis was performed using the FlowJo software v10.2 (Tree Star). Similarly, cells were analyzed for morphology and cell size using the Imaging Flow Cytometer ImageStreamX mark II (Amnis-EMD Millipore). Images were analyzed using the IDEAS 6.1 software (Amnis).

Determination of receptor expression levels

To evaluate surface receptor levels, cells were detached and washed twice in saline containing albumin (1%, w/v). Thereafter, cells were incubated for 30 min at 4°C using primary antibodies conjugated to fluorophores. Fluorescence intensity was measured using the BD FACSAria Fusion flow cytometer.

Cell proliferation assays

Proliferation of cells was assessed using XTT or MTT kits (from Biological Industries, Beit Haemek, Israel, or Sigma, respectively). Briefly, cells were seeded in triplicates in 96-well plates and treated for the indicated time intervals. Subsequently, MTT/XTT was added and following 3 h at 37°C, we dissolved in DMSO the water insoluble formazan crystals, which form in metabolically active cells. Optical density was measured at 570 nm. The MTT/XTT-based assays followed the manufacturer instructions.

Cell migration, invasion, and 3D assays

Cells were plated in the upper compartments of a Transwell tray (BD Biosciences) and allowed to migrate through the intervening membrane. Thereafter, cells were fixed in paraformaldehyde (3%), permeabilized in Triton X-100 (0.05%) and stained with crystal violet (0.02%). Cells on the upper side of the filter were removed and migrating cells were photographed. Invasion assays were performed using BioCoat Matrigel chambers. 3D spheroid cell invasion kits were from Trivigen. For trans-endothelial migration (TEM) assays, human umbilical vein endothelial cells (HUVEC) were grown to confluency on cell culture inserts. Tumor cells were added to the endothelial layer and left to transmigrate.

Clonogenic growth assay and adhesion assays

Cells were seeded in 6-well plates at a density of 1,000 cells per well. Appropriate treatments were given for the indicated time points, with medium change and fresh drug added every 2 days. Cells were fixed with 4% formaldehyde and stained with 0.5% crystal violet. Photos of stained cells were taken using an EPSON Perfection V600 scanner. Growth was quantified by dissolving crystal violet in 0.1% SDS and absorbance was quantified at 590 nm using a spectrophotometer. Signals were normalized to DMSO treatment. For adhesion tests, plates were coated overnight with Cultrex RGF BME (R&D Systems) or fibronectin, and gently washed thereafter (0.1% albumin in medium). Cells were allowed to adhere to the substrate for the indicated time points at 37°C. Unattached cells were removed and adherent cells were rinsed, fixed with paraformaldehyde (4%), and quantified after crystal violet staining (0.1%). The optical density was measured at 550 nm.

Immunofluorescence and live image analyses

Cells were grown on sterile 18 × 18 mm coverslips. Firstly, cells were washed in saline containing Tween 20 (0.01%; w/v). Thereafter, they were fixed in 4% formaldehyde. Fixed cells were incubated for 15 min in saline containing 0.1 M glycine, followed by a 30 min incubation in blocking buffer (10 mM Tris, pH 7.5, 150 mM NaCl, 10% goat serum, 2% albumin in Tris-buffered saline containing 0.2% Triton X-100). This was followed by 2 hours of incubation with the indicated primary antibodies (at cold), and diluted in the blocking buffer. Later, the cells were washed with saline and incubated with fluorescence-labelled secondary antibodies for 45 min. Subsequently, the cells were washed with saline and incubated for 5 min with Hoechst 33342 or DAPI. Next, cells were washed once again with saline and mounted on microscopic slides using an anti-quenching mounting media (Dako). The specimens were analyzed using a confocal laser-scanning microscope (LSM 800; Zeiss) equipped with a 63 Å/1.4 oil differential interference contrast M27 objective lens (Plan Apochromat; Carl Zeiss). We used the 488-, 543- and either 405- or 633-nm excitation wavelengths for fluorescein, Cy3 epifluorescence at 532-nm, and Cy5 at 647-nm and 4,6-diamidino-2- phenylindole (Hoechst). Images were ac-

quired using the LSM 800 software. Live imaging was performed using an Olympus IX83 epifluorescence microscope. FiJi (SciJava) software was used for title and time code labeling.

Immunofluorescence analyses

Cells were grown on sterile 18 × 18 mm coverslips. Firstly, cells were washed in saline containing Tween 20 (0.01%; w/v). Thereafter, they were fixed in 4% formaldehyde. Fixed cells were incubated for 15 min in saline containing 0.1 M glycine, followed by a 30 min incubation in blocking buffer (10 mM Tris, pH 7.5, 150 mM NaCl, 10% goat serum, 2% albumin in Tris-buffered saline and 0.2% Triton X-100), and then incubated for 2 hours with the indicated primary antibodies (at cold) and diluted in the blocking buffer. Later, the cells were washed with PBS and incubated with fluorescence-labelled secondary antibodies for 45 min. Subsequently the cells were washed with PBS and incubated for 5 min with Hoechst 33342 or DAPI, washed once again with PBS and mounted on microscopic slides using an anti-quenching mounting media (Dako). The specimens were analyzed using a confocal laser-scanning microscope (LSM 800; Zeiss) equipped with a 63 Å/1.4 oil differential interference contrast M27 objective lens (Plan Apochromat; Carl Zeiss) using the 488-, 543- and either 405- or 633-nm excitation wavelengths for fluorescein, Cy3 epifluorescence and either 4,6-diamidino-2- phenylindole (Hoechst) or Cy5, respectively. Images were acquired using the LSM 800 software.

Electron microscopy

We used the FEI Tecnai T12 TEM microscope (Thermo Fisher Scientific). MDA-MB-231 cells were fixed with 0.1% GA, 4% PFA, 3% sucrose in cacodilate buffer (0.1 M, pH 7.4) containing 5 mM $CaCl_2$. Next, ultrathin sections were cut and transferred to formvar-coated 200 mesh nickel grids.

Inter-species heterokaryon assays

A previously published protocol was used (Itahana et al., 2006). Accordingly, murine NIH3T3 (4×10^4) cells were transiently transfected with vector encoding ERK2-GFP and human HeLa cells (4×10^4) were transiently transfected with vector encoding NUP93. Twenty-four-hour post transfection, the cells were overlaid with an equal number of HeLa cells for 3 h in the presence of 100 μg/mL cycloheximide (Sigma). The transfectants were co-cultured and then fused with human HeLa cells in the presence of polyethylene glycol 1500 (50% (w/v) for 2 min. The solution was replaced with culture medium containing 100 μg/mL cycloheximide and further incubated for different time intervals. Interspecies heterokaryon cells were stained with Hoechst 33342 to help identify mouse and human nuclei.

Synthetic myristoylated peptides

Peptides were designed as mentioned before (Plotnikov et al., 2015). The following sequences were used: ERK Scramble, GNILSQELPHSGDLQIGL; ERK, GQLNHILGILGEPEQEDL; SMAD Scramble, MQSTPSGRVSISKCL; SMAD, KVLTQMGSPSIRCSS. All peptides were purchased from GenScript Ltd (Hong Kong).

Immunohistochemistry and picrosirius red staining

Formalin-fixed tumor sections were de-paraffinized and rehydrated. Antigen retrieval was performed in a microwave oven using a citric acid solution (pH 9.0). Slides were blocked in saline containing 20% horse serum, followed by treatment (15 min) with a blocking solution and an overnight incubation with the primary antibody. Thereafter, sections were incubated for 90 min with a biotinylated secondary antibody, followed by a Cy3-conjugated Streptavidin. DAPI was used to visualize nucleai. All slides were examined using a fluorescence microscope. Positive cells were counted using the Image Pro Plus software. For Picrosirius red staining, sections from tumor tissues were stained with 0.1% Picrosirius red and quantification was performed as above.

Invadopodia assays

Gelatin was labeled using Alexa Fluor 488 Protein Labeling Kit (Molecular Probes, Thermo Fisher Scientific). Glass-bottomed well plates were coated as mentioned above, with ratios of 1:10 labeled gelatin: non-labeled gelatin. Cells were plated on the gelatin matrix and cultured for varying lengths of time (on average, 5–6 h). Next, cells were fixed and stained for actin and DAPI, and degraded areas were assessed. Cells in every field of view were counted and the degradation area was calculated by the fluorescently labeled gelatin channel, using Analyze Particles plug-in (ImageJ software). Total degradation area/cell (μm^2) was used to assess invadopodia.

Rho GTPase activation assays and ELISA tests

G-LISA Small GTPase activation assays were performed by following the protocol of the activation assay kit (from Cytoskeleton). Human VEGF DuoSet, TGFB1-2 DuoSet and Human TGF-β RII DuoSet ELISA's were purchased from R&D Systems and assays were carried out as per the manufacturer's instructions.

Luciferase-reporter assays

Assays were performed as previously described (Srivastava et al., 2019). Briefly, cells were co-transfected with a luciferase reporter plasmid, along with control plasmids (Promega, Madison, WI). Luciferase activity was determined using the dual-luciferase reporter assay system (Promega). Firefly luciferase luminescence values were normalized to Renilla luminescence.

RNA isolation, real-time PCR analysis and RNA sequencing

The TRIzol reagent (Life Technologies) and the PerfectPure RNA Cultured Cells kit (5 Prime) were used for RNA purification and real-time quantitative PCR. Generation of cDNA was performed using either the qScript cDNA Synthesis kit (Quanta), High-capacity cDNA Reverse Transcription kit (Applied Biosystems), or RevertAid Reverse Transcriptase (Thermo Scientific). Real-time qPCR analysis was performed using Fast SYBR Green Master Mix (Applied Biosystems). Primers were designed using PrimerBlast. Transcripts encoding β-2 microglobulin (B2M) and glyceraldehyde-3-phosphate dehydrogenase (GAPDH) were used for normalization. Illumina HiSeq 2500v4 was used for RNA sequencing (~40 million reads per sample). Poly-A/T stretches and Illumina adapters were trimmed from the reads using Cutadapt. Reads were mapped to the Homo Sapiens GRCm38 reference genome using STAR (Dobin et al., 2013). Expression levels were quantified using htseq-count (Anders et al., 2015). Differentially expressed genes were identified using DESeq2 (Love et al., 2014) while employing betaPrior, cooksCutoff and independent filtering parameters set to False. Raw p values were adjusted for multiple testing using the procedure of Benjamini and Hochberg (Benjamini and Hochberg, 1995).

Extraction and sequencing of cytoplasmic and nuclear RNA

RNA extraction and analysis were performed as previously described (Zuckerman et al., 2020). Briefly, cells were washed in ice-cold PBS and detached from plates using 10 mM EDTA. A fraction was transferred to a new tube and RNA was extracted with TRIREAGENT (MRC). Remaining cells were washed in PBS, resuspended in RLN buffer (50 mM Tris-HCl pH 8.0, 140 mM NaCl, 1.5 mM $MgCl_2$, 10 mM EDTA, 1 mM DTT, 0.5% NP-40 and 10 U/mL RNase inhibitor), and incubated on ice for 5 min. The extract was centrifuged for 5 min at 300Xg in a cold centrifuge, the supernatant was transferred to a new tube, and centrifuged once again for 1 min at 500 g in a cold centrifuge. The supernatant (cytoplasmic fraction) was transferred to a new tube and RNA was extracted using TRIREAGENT. The nuclear pellet was washed once in RLN buffer, resuspended in 1 mL of buffer S1 (250 mM Sucrose, 10 mM $MgCl_2$, 10 U/mL RNase inhibitor), layered over 3 mL of buffer S3 (880 mM sucrose, 0.5 mM $MgCl_2$, 10 U/mL RNAse inhibitor), and centrifuged for 10 min at 2800Xg in a cold centrifuge. The supernatant was removed and RNA was extracted from the nuclear pellet using TRIREAGENT. Fractionation quality was validated by qRT-PCR using primers for ACTB and MALAT1, which are expected to be enriched in the cytosolic and the nuclear fractions, respectively. Cytosolic and nuclear fractions obtained after fractionation (from two biological replicates) were used to generate cDNA libraries using the SENSE mRNA-Seq Library Preparation kit (Lexogen) according to manufacturer's protocol and sequenced on a NextSeq 500 machine to obtain 75 nucleotide single-end reads. RNA-seq reads were mapped to the human genome (hg19 assembly) with STAR and gene expression levels were quantified using Bowtie2 and RSEM (Li and Dewey, 2011). GENCODE v26 annotations were used for further analysis. Differential expression in whole cell extract samples was computed using DESeq2 with default parameters. Subcellular localization was quantified similarly using DESeq2 and gene-level RSEM output.

Single molecule FISH

The protocol and probes we used have previously been described (Zuckerman et al., 2020). Probe libraries were designed according to Stellaris guidelines and synthetized by Stellaris (Stellaris RNA FISH probes, Biosearch Technologies). Libraries targeting NORAD consisted of 96 probes, labeled by Quasar® 570. Hybridizations were done overnight at 30°C with probes at a final concentration of 0.1 ng/μL. For nuclear staining, 1.25 μg/mL Hoechst 33342 (H3570, Thermo Fisher) was added during the washes. Images were taken with a Nikon Eclipse Ti2-E inverted fluorescence microscope equipped with an oil-immersion objective (X100) and an iXon 888 EMCCD camera using NIS-Elements Advanced Research software. The image-plane pixel dimension was 0.13 μm and distance between Z stacks was 0.3 μm. Quantification was done using FishQuant (Mueller et al., 2013). We performed automatic 2D projections as suggested in FishQuant documentation, followed by automatic cell segmentation using CellProfiler (McQuin et al., 2018). Hoechst signal was used to segment nuclei and the oligo-dT signal was used to segment cell bodies. Following batch analysis, we manually examined segmentation and removed incorrectly segmented cells from further analysis using the Fiji (ImageJ) software. Quantification of cytoplasmic and nuclear signals was performed with default parameters and recommended filters of FishQuant.

In vitro knockout of the gene encoding for NUP93

The CRISPR system was used as described (Ran et al., 2013) to create a double-stranded break next to the ProtospacerAdjacent Motif (PAM) sequence. The target site was selected from the ENSEMBL database in a way that targeted the transcript of NUP93. The selected target was 21 bp long, including the PAM sequence in exon 5, which was filtered to minimize off-target cross-reactivity. The sequence was cloned in pX458 and cells were sorted using cytometry.

Proteomic analysis

Proteins were digested and purified on carboxylated beads according to the SP3 protocol (Hughes et al., 2019). Peptides were analyzed by liquid-chromatography using the EASY-nLC1000 HPLC coupled to high-resolution mass spectrometric analysis on the Q-Exactive HF mass spectrometer (Thermo Fisher Scientific, Bremen, Germany). Peptides were separated on 50 cm EASY-spray columns (Thermo Fisher Scientific) with a single run of 140 min. MS acquisition was performed in a data-dependent mode with selection of the top 10 peptides from each MS spectrum for fragmentation and MS/MS analysis. Raw MS files were analyzed in the MaxQuant software and the Andromeda search engine (Cox et al., 2011). A database search was performed using the Uniprot database and included carbamidomethyl-cysteine as a fixed modification, as well as N-terminal acetylation and methionine oxidation as

variable modifications. A reverse decoy database was used to determine false discovery rate of 1% at the peptide and protein levels. The label-free algorithm (LFQ) in MaxQuant was used to retrieve the quantitative information. Nuclear and cytosolic proteins were quantified separately.

QUANTIFICATION AND STATISTICAL ANALYSIS

The statistical details of each assay appear in the relevant figure legends, including the statistical tests we used and the exact values of N. All data were analyzed using the Prism GraphPad software (version 8) and statistical analyses were performed using one- or two-way ANOVA with the Dunnett's or Tukey's test (*, $p \leq 0.05$; **, $p \leq 0.01$; ***, $p \leq 0.001$; ****, $p \leq 0.0001$). Data are presented as mean ± SEM. All experiments were carried out in triplicates, unless specified otherwise. All mass spectrometry statistical analyses were performed using the Perseus software (Tyanova et al., 2016). The MS data were filtered to include proteins with valid values in at least 75% of the samples. Missing values were then imputed to represent low abundance proteins by replacing them with random, low intensity values that form a normal distribution. Student t-test was performed (permutation-based, FDR = 0.05) to distinguish the significantly regulated proteins between the control and the NUP93-knockdown samples.